# An indicial-Polhamus aerodynamic model of insect-like flapping wings in hover

C.B. Pedersen & R. Żbikowski
*Department of Aerospace, Power & Sensors, Cranfield University (RMCS Shrivenham), Swindon SN6 8LA, UK.*

## Abstract

As part of the ongoing development of flapping-wing micro air vehicle prototypes at Cranfield University (Defence Academy Shrivenham), a model of insect-like wing aerodynamics in hover has been developed and implemented as MATLAB code. The model is intended to give better insight into the various aerodynamic effects on the wing, and therefore is as close to being purely analytical as possible. The model is modular, with the various effects treated separately. This modularity aids analysis and insight, and allows refinement of individual parts. However, it comes at the expense of considerable simplification, which requires empirical verification. The model starts from quasi-steady inviscid flow around a thin 2D rigid flat wing section, accounting for viscosity with the Kutta–Joukowski condition, and the leading edge suction analogy of Polhamus. Wake effects are modelled using the models of Küssner and Wagner, on a prescribed wake shape, as initially used by Loewy. The model has been validated against experimental data from Dickinson's Robofly and found to give acceptable accuracy. Some empirically inspired refinements of the Polhamus effect are outlined, but these need further empirical validation.

## 1 Introduction

This paper describes a novel aerodynamic model of insect-like flapping wings in hover, combining indicial methods of unsteady aerodynamics with Polhamus' leading edge suction analogy. The model has been derived for aerodynamic design of flapping wings of micro air vehicles (MAVs). MAVs are defined as flying vehicles ca. six inches in size (hand-held) and are developed to reconnoitre in confined spaces. Insect-like flapping entails reciprocal motion of pitching and plunging wings, and seems an attractive mode of propulsion for indoor flight at the MAV scale [1–3].

Phenomenologically, the interpretation of the flow dynamics involved, adopted here, is based on recent experimental evidence obtained by biologists from insect flight and related mechanical models. It is assumed that the flow is incompressible, has a low Reynolds number and is laminar

WIT Transactions on State of the Art in Science and Engineering, Vol 4, © 2006 WIT Press
www.witpress.com, ISSN 1755-8336 (on-line)
doi:10.2495/1-84564-095-0/6e

and that two factors dominate: (1) forces generated by the bound leading edge vortex, which models flow separation, and (2) forces due to the attached part of the flow generated by the periodic pitching, plunging and sweeping. The first of these resembles the analogous phenomenon observed on sharp-edged delta wings and is treated as such. The second contribution is similar to the unsteady aerodynamics of attached flow on helicopter rotor blades and is interpreted accordingly.

The indicial-Polhamus model is analytical and modular, and accounts for the main elements of the unsteady flow involved, i.e. (i) quasi-steady kinematic effects ('frozen' at each time), (ii) vortical lift (as on delta wings using the Polhamus model), (iii) unsteady kinematic effects (modelled using the Wagner function), (iv) shed wake effects (modelled using the Küssner function and corrections to the Wagner effect), and (v) added mass effects (non-circulatory lift due to acceleration of the surrounding air by the wings). This two-dimensional, wing-element model requires no empirical coefficients: given the required wing kinematics and geometry, all lift (drag) components are calculated and summed up to give the total lift (drag).

This aerodynamic model was implemented in MATLAB and runs in less than five minutes on a 1.8 GHz Pentium IV computer. The model's predictions have been verified on the best available set of experimental data, due to Dickinson. Despite several simplifying assumptions, lift prediction is quite good, while drag prediction is not as good.

Both from the insect flight analysis and MAV design perspectives there is a need for an analytic framework for aerodynamic modelling of flapping wings. It should offer qualitative and quantitative interpretations of the main phenomena involved while avoiding the extremes of mathematical oversimplification and intractable complexity. This problem is the main motivation for the developments presented here which were first suggested in [4] and subsequently developed in [5].

The main novel features of the proposed model are:

- wakeless solutions for quasi-steady and added mass Forces for the flapping motion, without assuming small angle of attack;
- a simplified, inviscid wake model for the effect of a highly curved wake filament, combining Wagner and Küssner functions with a modified Loewy model;
- a generalisation of the Polhamus leading edge suction analogy to include the effect of rapid pitching at large pitch angles;
- a method of calculating the force and moment of a wing, based on the kinematics of the tip, and a number of wing shape parameters;
- a code implementation of the above model.

This paper is organised as follows. This introduction continues by defining wing kinematics in Section 1.1 and commenting on aerodynamics of insect flight in Section 1.2. An overview of the proposed model is given in Section 2 to provide a roadmap for the core of the paper, Sections 3–6, in which the details of the model are derived. (The terminology for the derivations is in Appendix A.) A comment on code implementation follows in Section 7 and the data used to test the model's prediction are summarised in Section 8. The actual predictions are presented in Section 9 and discussed in Section 10. The paper ends with conclusions in Section 11.

### 1.1 Wing kinematics

Insects fly by oscillating (plunging) and rotating (pitching) their wings through large angles, while sweeping them forwards and backwards. The wingbeat cycle (typical frequency range: 5–200 Hz) can be divided into two phases: downstroke and upstroke (see Fig. 1). At the beginning of downstroke, the wing (as seen from the front of the insect) is in the uppermost and rearmost

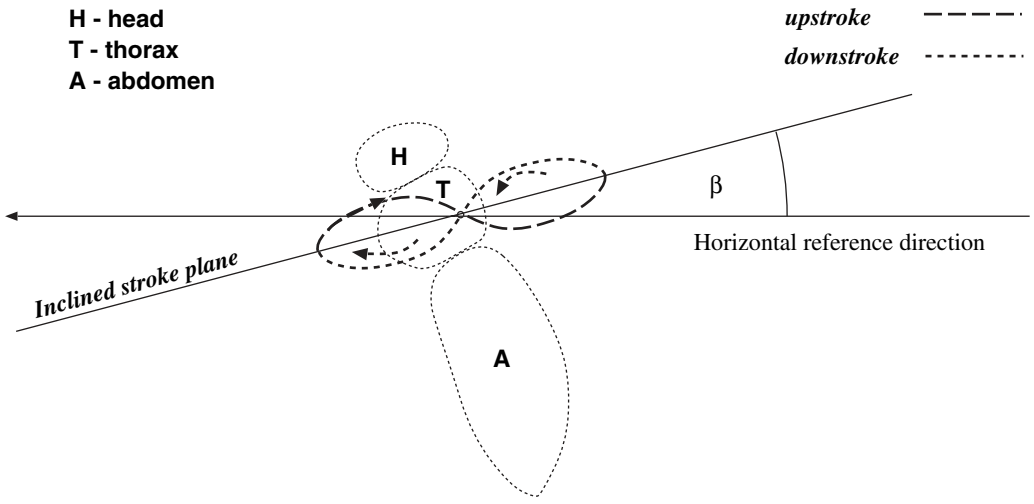


Figure 1: Typical motions of insect wing in hover. The insect body is oriented almost vertically, while the wing tip traces a flat figure of eight around the stroke plane. The stroke plane is inclined at an angle $\beta$.

position with the leading edge pointing forward. The wing is then pushed downwards (plunged) and forwards (swept) and rotated (pitched) with considerable change of the angle of attack at the end of the downstroke, when the wing is twisted rapidly, so that the leading edge points backwards, and the upstroke begins. During the upstroke the wing is pushed upwards and backwards and at the highest point the wing is twisted again, so that the leading edge points forward and the next downstroke begins.

Insect wing flapping occurs in a stroke plane that generally remains at the same orientation to the body and is either horizontal or inclined (see Fig. 1). In forward flight the downstroke lasts longer than the upstroke, because of the need to generate thrust. In hover they are equal, resulting in the wing tip typically tracing a flat figure of eight (as seen from the insect's side).

### 1.2 Main aerodynamic phenomena in insect flight

The kinematics of insect wings make the analysis of the associated aerodynamics a non-trivial task, not yet completed, especially in terms of its mathematical description. The classical approach, see e.g. [6], was based on the quasi-steady assumption that the instantaneous forces on the flapping wing are equivalent to those for steady motion at the same instantaneous velocity and angle of attack. However, Ellington in his seminal work [7–12] showed that this framework is inadequate to explain the high lift generated by insects, especially in hover (typically underestimating by a factor of three).

Ellington concluded that unsteady aerodynamics must be involved, but the nature of the unsteadiness was not clear. Subsequent experimental work [13–16] led to the remarkable discovery of a spiralling leading edge vortex in a large insect. This is a bound vortex, i.e. its position on the wing remains constant during a half-cycle, despite the wing's pitching, plunging and sweeping, while the vortex's size fluctuates. Inside the vortical structure spanwise flow (along the leading edge, from the wing base to the tip) was observed, an apparent cause of spiralling out of

the vortex. In hover, at the end of the downstroke the vortex is shed by a sudden wing twist and a new one is created symmetrically during the upstroke and shed when the wing flips again.

This persisting leading edge vortex was discovered through three-dimensional flow visualisation for a tethered hawkmoth *Manduca sexta* [14] and confirmed with a better resolution on an aerodynamically scaled up mechanical model of the hawkmoth [15, 16], powered by electric servomotors. Recent experiments on a mechanical model of the fruit fly *Drosophila melanogaster* wing by Dickinson [17] seem to suggest that a bound leading edge vortex also occurs on smaller insects. However, the spanwise spiralling out, detected by Ellington *et al.* for the hawkmoth, was observed to be weak.

The interpretation of the above biological results, adopted here, is taken from [4]. We assume that the main aerodynamic phenomena occurring in insect-like flapping are:

1. bound leading edge vortex, persisting during each half-cycle and shed at the end of it,
2. effects (other than the vortex) of wing pitching, plunging and sweeping are present all the time, and
3. wing interaction with its own convected wake (caused by previous wingbeats) due to its forward–backward sweeping (re-entering the wake).

The flow is assumed incompressible, has a low Reynolds number and is laminar, while the wing is treated as rigid, thin and of symmetrical section. These postulates are well supported in experimental observation of insect flight, with the exception of wing rigidity.

Because the flow is laminar, it is susceptible to separation and it is hypothesised here that insects deliberately provoke separation at the leading edge to exploit the vortical lift thus obtained. It is also postulated that no further separation occurs during each half-cycle and that the vortex is shed at the end of it, due to a sudden wing flip. Hence, the starting point of the proposed conceptual framework is to interpret phenomenon (1) as accounting for the *separated* part of the flow, while treating (2) as responsible for the *attached* part of the flow interacting with (3), i.e. no interaction between (1) and (3). This important division is also the first indirect inclusion of the effect of viscosity, by allowing for the bound leading edge vortex. The unsteady contributions of the non-vortical part of the flow will be analysed as inviscid, but with the imposition of the Kutta condition on the trailing edge which takes into account viscosity for the second (and last) time. There is some controversy in the literature, see e.g. [18], whether the Kutta condition is indeed valid for unsteady flows. The developments presented here rely on extensively verified, e.g. [19], aerodynamic modelling of unsteady wing motions where the validity seems to hold.

The vortical lift due to (1) is interpreted as essentially identical to the leading edge vortex on sharp-edged delta wings, see [20, 21], *not* as dynamic stall, as in [22]. The reasons for this are now explained.

Pitching, plunging and sweeping wings are well known in helicopter rotor design, see [23], and their aerodynamics can be derived from unsteady thin aerofoil theory, provided the flow is attached. For helicopter blades this cannot be guaranteed for angles of attack $\alpha$ in excess of $15°$, for then separation begins. If $\alpha$ continues to increase between $15° \leq \alpha \leq 20°$, dynamic stall develops, see [22]. This is characterised by a vortex arising initially at the leading edge, but soon being convected over the chord to be shed from the trailing edge at $\alpha \approx 20°$. This shedding is accompanied by a catastrophic loss of lift due to a massive flow separation on the whole wing. It should be emphasised that if the angle of attack *continually* increases from $15°$ to $20°$, the vortex is *never* bound and is constantly being convected towards the trailing edge.

In contrast, in every half-cycle of insect-like flapping $\alpha$ is well above $20°$ and the leading edge vortex is still bound. This is because separation occurs at the beginning of the motion and keeps generating stable vortical lift throughout the half-cycle of the motion. Over a half-cycle, it is not

a transient phenomenon leading to a catastrophic loss of lift. Moreover, this controlled separation remains localised at the leading edge (unlike in dynamic stall) and occurs nowhere else on the wing, so that the rest of the wing flow is *attached*.

Thus, the essence of the framework proposed here is to account separately for the bound leading edge vortex and for the other (attached) part of the flow, and then adding both contributions.

## 2 Model overview and relevant prior work

Following the flow phenomenology explained in Section 1.2, the proposed model is modular, accounting separately for the appropriate constituent elements of the flow (see Fig. 2). The wing is divided into rectangular elements and the appropriate contributions of each element are then summed up to produce the total aerodynamic force. The model is thus essentially two-dimensional.

### 2.1 Model structure and assumptions

The model starts with the inviscid flow around a thin, flat wing section in two dimensions, using thin aerofoil theory (see Chapter 4 of [20]). The velocity potential is used to derive the quasi-steady forces in Section 3, and again for the added mass forces in Section 4. The standard unsteady aerodynamics approach is followed, see [23], but extra terms are included for the velocity due to significant wing rotation.

The separated flow at the sharp leading edge is modelled using the Polhamus leading edge suction analogy, [24], as detailed in Section 5. The model assumes that any leading edge suction is rotated through 90° to become an additional normal force.

Simple modelling of wake effects is the main thrust of this work, a problem dealt with in Section 6. Briefly, wake effects usually attenuate changes in forces, as the shed vorticity will oppose the creation of vorticity bound to the wing. The wake is treated as a thin filament of vorticity shed from the trailing edge, and the effect is expressed analytically using simplified wake models. First amongst these is the Wagner function, see [25], which deals with the effect of a two-dimensional straight-line wake behind an arbitrarily pitching and accelerating aerofoil. The Küssner function, see [26], deals with a similar case, but for a change in lift coefficient due to a gust, which the wing gradually enters as it moves. Since we focus on hover, the wake will remain in the vicinity of the wing, but will move downwards over time. Loewy [27] modelled the wake of a hovering rotorcraft by splitting the wake into straight-line elements: a primary wake behind

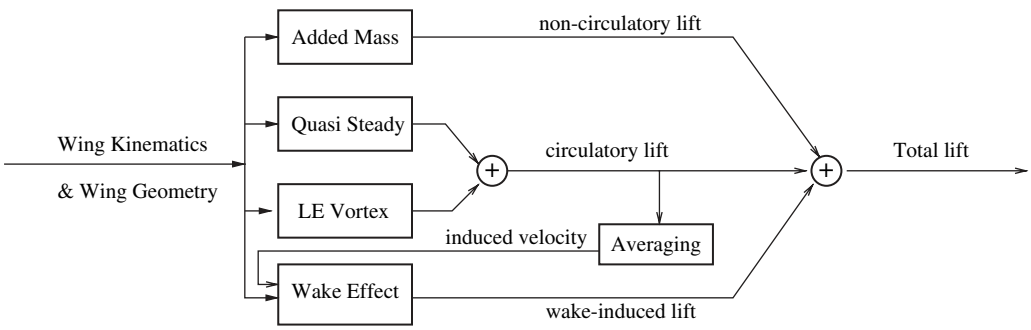


Figure 2: Overview of the modular method for modelling the aerodynamic effects. Note the lack of iterative loops: only one-pass computation is required.

the wing, and a series of straight-line secondary wakes below the wing. This model is adapted for use with flapping flight.

The main simplifying assumptions made are:

1. The wing is thin and flat.
2. The flow is stationary for purposes of force calculations.
3. The flow is inviscid.
4. The effect of the leading edge vortex is to rotate the leading edge suction force by 90°.
5. The leading edge vortex dissipates immediately when shed.
6. The flow leaves the trailing edge smoothly, satisfying the Kutta–Joukowski condition.
7. The wake is treated as a thin, globally stationary filament of vorticity, which has no self-induced velocity effects.
8. The wake is split into single-stroke elements, assumed to be straight lines.
9. The wake moves under constant downwash velocity $u_i$, without deforming under its own induced velocity.

Also, only the Polhamus model of the leading edge vortex accounts for flow separation. The rest of the model assumes the flow to be attached.

### 2.2 Relevant prior work

While new, this is not the first model to attempt to separate the contributions of various aerodynamic effects in order to create a modular model. We highlight only the most relevant examples, since reviews of greater scope have appeared recently [28–30].

The early work of Ellington [11] proposed the pulsed actuator disc model of the wake, which simply models the wake as a series of vortex rings, shed once per stroke, and convected downwards by a constant downwash velocity. Ellington then applied this effect as a correction to the average lift during a cycle. Although this is a good first-order model, in that it correctly identifies the general shape of the wake vorticity, it does not model the unsteady lift profile during the individual strokes.

In a later development, Walker [31] modelled the lift of the wing through elements using the aerofoil section formula $F = \rho U \Gamma$, where $U$ is the forward velocity of the wing. Walker then treated the bound vorticity of the wing $\Gamma$ as a superposition of four circulation components, similarly to this method. However, he introduced empirical corrections to the vorticity which would have to be obtained a new each time the design is modified. Such semi-empirical approaches also have the disadvantage of lumping together, in an unknown way, disparate aerodynamic effects by representing them through an amalgamated measurement. This is avoided in the model developed here, where each lift component is clearly identified and precisely derived.

The work closest to ours is Minotti [32]. However, the two main differences are: (1) for leading edge vortex modelling he uses a point vortex placed in an arbitrary position above the wing; (2) the attached part of the flow is not decomposed into quasi-steady, wake-related and added mass components, as in our study.

## 3 Quasi-steady effects

The following sections make extensive use of the mathematical definitions in Appendix A.

### 3.1 Potential theory

A two-dimensional potential model of the inviscid flow around a thin, flat aerofoil is used to form a complex velocity potential $\bar{\Phi}$, which has the property of differentiating to the velocity of the flowfield: $d\bar{\Phi}/d\bar{z} = u_P - iu_N$. For the case of a thin, flat plate, the potential is purely real, as a function of the wing coordinate $\zeta$ only: $\Phi = \Phi(\zeta)$.

Some standard results of potential theory, e.g. [33], are:

1. The potential due to a bound vorticity $\gamma$ is such that $\partial\Phi/\partial x = \gamma$.
2. The datum of $\Phi$ can be set arbitrarily.
3. Individual $\Phi$ for several flowfields can be superimposed, to give their combined effect.

The following identity

$$\frac{\partial\Phi}{\partial\zeta} = b\gamma \tag{1}$$

and the quantity $Q = \sqrt{1-\zeta^2}$ will be used extensively.

### 3.2 Dirichlet solution

The Dirichlet solution is the potential function needed to cancel out the component of the local free stream velocity normal to the surface of the wing, making the wing surface a streamline. It does this without contributing a net circulation to the flow. This is also the minimum energy solution to the problem, i.e. it is the solution that imparts the least amount of kinetic energy to the fluid. This has been done in a variety of ways. von Kármán and Sears [34] directly wrote the bound $\gamma$ needed. Theodorsen [35] formed the potential function from a set of source–sink pairs on the upper and lower surface of a unit circle, then used Joukowski mapping to map the circle to a straight line, where the source–sink pairs become doublets aligned normally to the wing. Finally, Katz and Plotkin [33] wrote the expression for the doublet strength needed directly, then showed that this could be differentiated to give the bound vorticity.

Whichever method is used, the end result is a potential function split into two superposable parts: one for the translational motion, and one for the rotation about the hinge line (pitch axis). The potential on the upper surface is:

$$\Phi^+_{TD} = u_N bQ, \tag{2}$$

$$\Phi^+_{RD} = \dot{\beta}b^2\left(\frac{\zeta Q}{2} - aQ\right). \tag{3}$$

For this the ability to define the datum of $\Phi$ arbitrarily was used, so the potential on the upper and lower surface are exactly equal and opposite.

$\Phi^+$ can be differentiated to give the bound vorticity:

$$\gamma^+_{TD} = u_N b\frac{-\zeta}{Q}, \tag{4}$$

$$\gamma^+_{RD} = \dot{\beta}b^2(\tfrac{1}{2} - \zeta^2 + a\zeta)/Q. \tag{5}$$

There are two singularities, one each at the leading edge and trailing edge. At these points $\gamma$ and velocity become infinite, and $\Phi$ is discontinuous unless zero. This is dealt with in Sections 3.3 and 3.6.

### 3.3 Kutta–Joukowski condition

Kutta and Joukowski independently observed that the discontinuity at the trailing edge is equivalent to the flow passing around the trailing edge, experiencing infinite acceleration as it does. In a real fluid, the flow will be unable to do this, and will instead separate at the trailing edge. Satisfying the Kutta–Joukowski condition involves superposing a net bound vorticity onto the Dirichlet solution, so the flow leaves smoothly at the trailing edge. The correction required to satisfy this condition is referred to in this work as the Kutta–Joukowski correction. It is an empirically-inspired correction to the potential flow model, to make the flow behave like a real, viscous fluid. This additional vorticity should not cause any net normal flow anywhere on the wing, so the wing remains a streamline.

Derivation of the Kutta–Joukowski condition can be approached from the potential or vorticity perspective. van Kármán and sears [34] write the expression for the vorticity needed to cancel the velocity at the trailing edge directly. Note, however, that their solution includes the vorticity of the shed wake, which will be dealt with as a separate effect in the model. Theodorsen [35] uses a uniform distribution of vorticity about a unit circle of sufficient strength to cancel the Dirichlet potential at the trailing edge, then maps this to a line. Katz and Plotkin [33] write the vorticity needed directly.

For the wake-free case, the latter two methods give expressions for potential and vorticity:

$$\Phi^{+}_{\mathrm{TK}} = u_{\mathrm{N}} b(a \sin(\zeta) - \pi/2), \tag{6}$$

$$\Phi^{+}_{\mathrm{RK}} = \dot{\beta} b^2 \left(\tfrac{1}{2} - a\right)(a \sin(\zeta) - \pi/2), \tag{7}$$

$$\gamma^{+}_{\mathrm{TK}} = u_{\mathrm{N}} b/Q, \tag{8}$$

$$\gamma^{+}_{\mathrm{RK}} = \dot{\beta} b^2 \left(\tfrac{1}{2} - a\right)/Q, \tag{9}$$

where the expressions have been split into a translational and a rotational part, as above.

The discontinuity at the leading edge still exists; this is dealt with in Section 5 using leading edge suction, and the Polhamus leading edge suction analogy.

### 3.4 Unsteady form of Bernoulli equation

The well-known unsteady Bernoulli equation, see e.g. [33], is:

$$p = \rho \left( p_0(t) + \frac{\partial \Phi}{\partial t} - \frac{1}{2} u^2_{\mathbf{T}\mathrm{Ef}} \right). \tag{10}$$

The $\partial\Phi/\partial t$ term is the added mass, which will be dealt with in Section 4. The last term becomes the quasi-steady pressure. The velocity of a fluid particle on the upper surface $u^{+}_{\mathbf{T}\mathrm{Ef}}$, is written as:

$$u^{+}_{\mathbf{T}\mathrm{Ef}} = (u_{\mathrm{P}} + u_{\mathrm{P}\gamma} + i u_{\mathrm{NE}}), \tag{11}$$

where $u_{\mathrm{P}}$ is the velocity of the undisturbed free stream relative to the wing, $u_{\mathrm{P}\gamma}$ is the additional velocity relative to the wing, caused by the bound vorticity. This velocity is purely parallel to the wing surface, and equals $\partial\Phi/\partial\zeta$ and $\gamma$. The square of this velocity $\bar{u}^{2+}_{\mathbf{T}}$ is obtained by substituting

$\gamma$ for $u_{\mathrm{P}\gamma}$:

$$u^{2+}_{\mathrm{TEf}} = (u_{\mathrm{P}} + \gamma + iu_{\mathrm{NE}})(u_{\mathrm{P}} + \gamma - iu_{\mathrm{NE}}) \tag{12}$$

$$= u^2_{\mathrm{P}} + \gamma^2 + u^2_{\mathrm{NE}} + 2\gamma u_{\mathrm{P}}. \tag{13}$$

Consider the pressure difference across the wing $\Delta p$. The stagnation pressure $p_0$ is the same above and below. The first three terms of the above are the velocity of the wing, which is the same above and below, so they cancel, yielding:

$$\Delta p_{\mathrm{Q}} = -\rho \tfrac{1}{2} 2u_{\mathrm{P}}\gamma^+ - \rho \tfrac{1}{2} 2u_{\mathrm{P}}\gamma^-$$

$$= -2\rho u_{\mathrm{P}}\gamma^+. \tag{14}$$

This gives the normal force for a unit spanwise element of the wing as:

$$dF_{\mathrm{NQ}} = 2\rho u_{\mathrm{P}}\gamma^+ d\zeta$$

$$= \rho u_{\mathrm{P}}\gamma d\zeta. \tag{15}$$

This is a familiar result: a uniform free stream flowing past a vortex will cause a force normal to the flow, of a magnitude proportional to the product of the velocity and the circulation.

### 3.5 Leading edge suction correction

The result of eqn (15) is used to incorporate the effect of leading edge suction, by substituting the total velocity for the parallel velocity, so that

$$dF_{\mathrm{NQ}} + idF_{\mathrm{PQ}} = \rho \bar{u}_{\mathrm{TE}} \gamma \, d\zeta, \tag{16}$$

where $dF$ is the increment of force corresponding to the increment of chord length $d\zeta$ and the total velocity of the wing is $u_{\mathrm{TE}} = u_{\mathrm{P}} + iu_{\mathrm{N}} + i\dot{\beta}b\zeta - I\dot{\beta}ba$. The total force is normal to the total velocity.

### 3.6 Quasi-steady forces

The quasi-steady forces on the wing are found for each of the $\gamma$ components calculated above, using standard integrals of the parameter $Q$. The values for $\gamma$ employed here are twice those for $\gamma^+$ given earlier, as explained above. This calculation differs from the standard textbook case, in that the rotational component of normal velocity $i\dot{\beta}b(\zeta - a)$, is not neglected here, since it is not small compared to the translational velocity. This is because this application has low translational velocity and high angle of attack. For clarity, the solution is split into four components: The cases of isolated translation ($T$) and rotation ($R$), for the Dirichlet (D) and Kutta–Joukowski (K) potentials:

TD part:

$$F_{\mathrm{NQ}} + iF_{\mathrm{PQ}} = \rho \int_{-1}^{1} \bar{u}_{\mathrm{TE}} \gamma_{\mathrm{TD}} \, d\zeta = 2\rho b u_{\mathrm{N}} \int_{-1}^{1} \bar{u}_{\mathrm{TE}} \frac{-\zeta}{Q} \, d\zeta$$

$$= -\pi \rho b^2 u_{\mathrm{N}} \dot{\beta} \tag{17}$$

RD part:

$$F_{\mathrm{NQ}} + iF_{\mathrm{PQ}} = \rho \int_{-1}^{1} \bar{u}_{\mathbf{T}\mathrm{E}} \gamma_{\mathrm{RD}}\, d\zeta = 2\rho b^2 \dot{\beta} \int_{-1}^{1} \bar{u}_{\mathbf{T}\mathrm{E}} \left(\tfrac{1}{2} - \zeta^2 + a\zeta\right)/Q\, d\zeta$$
$$= \pi\rho b^2 u_{\mathrm{N}} \dot{\beta} \tag{18}$$

The total quasi-steady contribution of the Dirichlet part is zero, which is as expected: since there is no net vorticity, there can be no net force.

TK part:

$$F_{\mathrm{NQ}} + iF_{\mathrm{PQ}} = \rho \int_{-1}^{1} \bar{u}_{\mathbf{T}\mathrm{E}} \gamma_{\mathrm{TK}}\, d\zeta = 2\rho b u_{\mathrm{N}} \int_{-1}^{1} \bar{u}_{\mathbf{T}\mathrm{E}} \frac{1}{Q}\, d\zeta$$
$$= 2\pi\rho b u_{\mathrm{N}} \bar{u}_{\mathbf{T}\mathrm{m}}. \tag{19}$$

RK part:

$$F_{\mathrm{NQ}} + iF_{\mathrm{PQ}} = \rho \int_{-1}^{1} \bar{u}_{\mathbf{T}\mathrm{E}} \gamma_{\mathrm{RK}}\, d\zeta = 2\rho b^2 \left(\tfrac{1}{2} - a\right) \dot{\beta} \int_{-1}^{1} \bar{u}_{\mathbf{T}\mathrm{E}}/Q\, d\zeta$$
$$= 2\pi\rho b^2 \dot{\beta} \left(\tfrac{1}{2} - a\right) \bar{u}_{\mathbf{T}\mathrm{m}}. \tag{20}$$

The Kutta–Joukowski components produce net forces, because they have a net vorticity.

### 3.7 Total quasi-steady force

The total quasi-steady force is written as the sum of the four components given in eqns (17)–(20):

$$F_{\mathrm{NQ}} + iF_{\mathrm{PQ}} = 2\pi\rho b\, (u_{\mathrm{N}} \bar{u}_{\mathbf{T}\mathrm{m}} + b\, \dot{\beta}(\tfrac{1}{2} - a)\bar{u}_{\mathbf{T}\mathrm{m}}) \tag{21}$$
$$= 2\pi\rho b u_{\mathrm{Nr}} \bar{u}_{\mathbf{T}\mathrm{m}}, \tag{22}$$

where the normal and parallel components are:

$$F_{\mathrm{NQ}} = 2\pi\rho b u_{\mathrm{Nr}} u_{\mathrm{P}} \tag{23}$$
$$F_{\mathrm{PQ}} = 2\pi\rho b u_{\mathrm{Nr}} u_{\mathrm{Nm}}. \tag{24}$$

The horizontal and vertical components of these forces are:

$$F_{\mathrm{HQ}} = -F_{\mathrm{NQ}}\mathbf{S}_\beta + F_{\mathrm{PQ}}\mathbf{C}_\beta = 2\pi\rho b u_{\mathrm{Nr}}(-u_{\mathrm{P}}\mathbf{S}_\beta + u_{\mathrm{Nm}}\mathbf{C}_\beta)$$
$$= 2\pi\rho b u_{\mathrm{Nr}} u_{\mathrm{Vm}}, \tag{25}$$
$$F_{\mathrm{VQ}} = F_{\mathrm{NQ}}\mathbf{C}_\beta + F_{\mathrm{PQ}}\mathbf{S}_\beta = 2\pi\rho b\, u_{\mathrm{Nr}}(u_{\mathrm{P}}\mathbf{C}_\beta + u_{\mathrm{Nm}}\mathbf{S}_\beta)$$
$$= 2\pi\rho b u_{\mathrm{Nr}} u_{\mathrm{Hm}}. \tag{26}$$

Mapping from spherical to rectangular coordinates, the force on the wing is:

$$L = F_{\mathrm{VQ}}\mathbf{C}_\psi, \tag{27}$$
$$D = F_{\mathrm{HQ}}\mathbf{S}_\theta. \tag{28}$$

Recall that drag is defined as force in the $+x$ direction, not the direction opposing motion.

The standard results are recovered readily by making the same assumptions about fast forward motion at low angle of attack, i.e. that $\beta$ is small, and $\theta, \psi = 0$. In this case, $u_{\mathrm{P}} \approx u_{\mathrm{H}}$, and the lift force will be the normal force:

$$L = 2\pi\rho b u_{\mathrm{Nr}} u_{\mathrm{H}}. \tag{29}$$

This is indeed the standard result for a pitching aerofoil at low $\beta$.

### 3.8 Wing integrals

The above calculations are forces per unit span. This is now extended to the force for the entire wing by integrating along the span, using two-dimensional strip theory:

$$\begin{aligned} F_{\mathrm{NQW}} &= R\int_0^1 F_{\mathrm{NQ}}\,dr \\ &= \rho R\int_0^1 b u_{\mathrm{P}} u_{\mathrm{N}}\,dr + \rho R\int_0^1 b^2 u_{\mathrm{P}}\dot{\beta}\left(\tfrac{1}{2}-a\right)dr. \end{aligned} \tag{30}$$

It follows from the first term that the velocities at the pitch axis scale directly with $r$, so they can be written in terms of the tip velocities and $r$:

$$\begin{aligned} \int_0^1 b u_{\mathrm{P}} u_{\mathrm{N}}\,dr &= \int_0^1 br u_{\mathrm{PT}} r u_{\mathrm{NT}}\,dr \\ &= u_{\mathrm{PT}} u_{\mathrm{NT}}\int_0^1 br^2\,dr. \end{aligned} \tag{31}$$

Also, the semichord $b$ can be expressed as a fraction of the maximum semichord $B$:

$$\begin{aligned} u_{\mathrm{PT}} u_{\mathrm{NT}}\int_0^1 br^2\,dr &= u_{\mathrm{PT}} u_{\mathrm{NT}} B\int_0^1 \frac{b}{B} r^2\,dr \\ &= u_{\mathrm{PT}} u_{\mathrm{NT}} B\, b_1 r_2. \end{aligned} \tag{32}$$

The term $b_1 r_2$ is defined as the integral $\int_0^1 (b/B) r^2\,dr$; the subscripts are the powers of $b/B$ and $r$, respectively. Thus the integral is purely a function of the wing shape, not the wing scale. These so-called wing shape factors are convenient in that they speed up calculation considerably, and give additional insight into how the wing shape affects the forces.

Now consider the second term:

$$\begin{aligned} \int_0^1 b^2 u_{\mathrm{P}}\dot{\beta}\left(\tfrac{1}{2}-a\right)\,dr &= \dot{\beta} u_{\mathrm{PT}} B^2\int_0^1 \left(\tfrac{1}{2}-a\right)\left(\frac{b}{B}\right)^2 r\,dr \\ &= \dot{\beta} u_{\mathrm{PT}} B^2\left[\tfrac{1}{2} b_2 r_1 - b_2 r_{1a}\right], \end{aligned} \tag{33}$$

where $b_2 r_1 = \int_0^1 (b/B)^2 r\,dr$, and $b_2 r_{1a} = \int_0^1 (b/B)^2 r a\,dr$.

Assuming $a$ is constant along the span, eqn (33) can be simplified to:

$$\begin{aligned} \int_0^1 b^2 u_{\mathrm{P}}\dot{\beta}\left(\tfrac{1}{2}-a\right)\,dr &= \dot{\beta} u_{\mathrm{PT}} B^2\left(\tfrac{1}{2}-a\right)\int_0^1 \left(\frac{b}{B}\right)^2 r\,dr \\ &= \dot{\beta} u_{\mathrm{PT}} B^2\left(\tfrac{1}{2}-a\right) b_2 r_1. \end{aligned} \tag{34}$$

The total force on the wing, assuming that $a$ is constant along the span, is

$$F_{\mathrm{NQW}} = R\int_0^1 F_{\mathrm{NQ}}\,dr$$
$$= 2\pi\rho RB\,u_{\mathrm{PT}}\left[\,u_{\mathrm{NT}}\,b_1 r_2 + \dot{\beta}B\,\left(\tfrac{1}{2}-a\right)\,b_2 r_1\right], \tag{35}$$

$$F_{\mathrm{PQW}} = R\int_0^1 F_{\mathrm{PQ}}\,dr$$
$$= 2\pi\rho RB\left[u_{\mathrm{NT}}^2 b_1 r_2 + u_{\mathrm{NT}}B\dot{\beta}\left(\tfrac{1}{2}-2a\right)b_2 r_1 + b^2\dot{\beta}^2 a^2 b_3 r_0\right]. \tag{36}$$

### 3.9 Moments

The vertical ($M_{\mathrm{VQ}}$) and horizontal moments ($M_{\mathrm{HQ}}$) are:

$$M_{\mathrm{VQ}} = RF_{\mathrm{VQ}}r, \tag{37}$$
$$M_{\mathrm{HQ}} = RF_{\mathrm{HQ}}r. \tag{38}$$

The pitching moment about the hinge is formed by going back to the original integral of normal force along the chord and multiplying by the offset from the hinge $b(a-\zeta)$.

$$M_{\beta\mathrm{Q}} = \rho\int_{-1}^{1}\gamma u_{\mathrm{P}}b\,(a-\zeta)\,d\zeta. \tag{39}$$

Equation (39) is now applied to the components of $\gamma$ in eqns (4), (5), (8) and (9):

TD part:

$$M_{\beta\mathrm{QTD}} = \rho\int_{-1}^{1}\gamma_{\mathrm{TD}}u_{\mathrm{P}}b\,(a-\zeta)\,d\zeta = 2\rho u_{\mathrm{N}}u_{\mathrm{P}}b^2\int_{-1}^{1}\frac{-\zeta}{Q}\,(a-\zeta)\,d\zeta$$
$$= \pi\rho u_{\mathrm{N}}u_{\mathrm{P}}b^2. \tag{40}$$

RD part:

$$M_{\beta\mathrm{QRD}} = \rho\int_{-1}^{1}\gamma_{\mathrm{RD}}u_{\mathrm{P}}b\,(a-\zeta)\;d\zeta$$
$$= 2\rho\dot{\beta}u_{\mathrm{P}}b^3\int_{-1}^{1}\frac{\left(\frac{1}{2}-\zeta^2+a\zeta\right)(a-\zeta)}{Q}\,d\zeta$$
$$= -\pi\rho\dot{\beta}u_{\mathrm{P}}b^3 a. \tag{41}$$

TK part:

$$M_{\beta\mathrm{QTK}} = \rho\int_{-1}^{1}\gamma_{\mathrm{TK}}u_{\mathrm{P}}b\,(a-\zeta)\;d\zeta = 2\rho u_{\mathrm{N}}u_{\mathrm{P}}b^2\int_{-1}^{1}\frac{a-\zeta}{Q}\,d\zeta$$
$$= 2\pi\rho u_{\mathrm{N}}u_{\mathrm{P}}b^2 a. \tag{42}$$

RK part:

$$M_{\beta\mathrm{QRK}} = \rho \int_{-1}^{1} \gamma_{\mathrm{RK}} u_{\mathrm{P}} b\,(a-\zeta)\,d\zeta = 2\rho\dot{\beta} u_{\mathrm{P}} b^3 \int_{-1}^{1} \frac{\frac{1}{2}a - a^2 - \frac{1}{2}\zeta + a\zeta}{Q}\,d\zeta$$

$$= \pi\rho\dot{\beta} u_{\mathrm{P}} b^3 (a - 2a^2). \tag{43}$$

Total moment:

$$M_{\beta\mathrm{Q}} = M_{\beta\mathrm{QTD}} + M_{\beta\mathrm{QRD}} + M_{\beta\mathrm{QTK}} + M_{\beta\mathrm{QRK}}$$

$$= \pi\rho b^2 u_{\mathrm{P}} \left(u_{\mathrm{N}}\,(1+2a) - \dot{\beta} b a^2\right). \tag{44}$$

The expressions for $M_{\mathrm{VQ}}$ and $M_{\mathrm{HQ}}$ bear considerable similarity to the force expressions, but the pitching moment expression does not, due to the extra factor of $\zeta$ it introduces.

### 3.10 Wing moment integrals

We proceed as in Section 3.8: the wing integrals are written in terms of shape parameters, assuming the hinge location to be constant.

$$M_{\mathrm{VQ}} = RF_{\mathrm{VQ}} r,$$

$$M_{\mathrm{VQW}} = R^2 \int_0^1 F_{\mathrm{VQ}} r\,dr$$

$$= 2\pi\rho R^2 B\, u_{\mathrm{NT}}\, u_{\mathrm{HT}}\, b_1 r_3 + 2\pi\rho R^2 B^2 u_{\mathrm{NT}} \dot{\beta} a \mathbf{S}_\beta b_2 r_2$$

$$+ 2\pi\rho R^2 B^2 u_{\mathrm{HT}} \dot{\beta} \left(\tfrac{1}{2} - a\right) b_2 r_2 + 2\pi\rho R^2 B^3 \dot{\beta}^2 \left(\tfrac{1}{2}a - a^2\right) \mathbf{S}_\beta b_3 r_1, \tag{45}$$

$$M_{\mathrm{HQ}} = RF_{\mathrm{HQ}} r,$$

$$M_{\mathrm{HQW}} = R^2 \int_0^1 F_{\mathrm{VQ}} r\,dr$$

$$= 2\pi\rho R^2 B\, u_{\mathrm{NT}}\, u_{\mathrm{VT}}\, b_1 r_3 + 2\pi\rho R^2 B^2 u_{\mathrm{NT}} \dot{\beta} a \mathbf{C}_\beta b_2 r_2$$

$$+ 2\pi\rho R^2 B^2 u_{\mathrm{VT}}\, \dot{\beta} \left(\tfrac{1}{2} - a\right) b_2 r_2 + 2\pi\rho R^2 B^3 \dot{\beta}^2 \left(\tfrac{1}{2}a - a^2\right) \mathbf{C}_\beta b_3 r_1, \tag{46}$$

$$M_{\beta\mathrm{Q}} = \pi\rho b^2 u_{\mathrm{P}} \left(u_{\mathrm{N}}\,(1+2a) - \dot{\beta} b a^2\right)$$

$$M_{\beta\mathrm{QW}} = \pi\rho R \int_0^1 u_{\mathrm{P}} b^2 \left(u_{\mathrm{N}}\,(1+2a) - \dot{\beta} b a^2\right) dr$$

$$= \pi\rho R B^2\, u_{\mathrm{PT}} \left(u_{\mathrm{NT}}\,(1+2a)\, b_2 r_2 - \dot{\beta} B a^2 b_3 r_1\right). \tag{47}$$

## 4 Added mass effects

### 4.1 What is added mass?

Long ago Stokes [36] showed experimentally that the force on a pendulum in a fluid depended not only on the speed of the pendulum, but also the acceleration. When a body is accelerated in a fluid, it will experience a retarding force, apart from the viscous drag. This is completely independent of the inertia of the body itself and can be shown to occur even in a completely inviscid fluid for a massless object. This is called an *irrotational* or *non-circulatory* effect, because it does not rely on a net circulation in order to generate force. However, net circulatory components will also have an added mass effect, since adding them will modify the potential, see e.g. [35].

The concept of forces arising from an inviscid fluid is somewhat counterintuitive, so we offer a brief explanation of that effect, inspired by [37]. Suppose a body is moving with a velocity $U$ through an undisturbed, inviscid fluid. In order to allow the body to pass, fluid has to move aside ahead of the body and close up after it. Thus, the fluid acquires kinetic energy due to the passage of the body, even when the free stream is at rest. When $U$ is constant, this kinetic energy is also constant and there is no net force on the body, as expected. However, increasing the velocity of the body will also increase the kinetic energy of the flow, so the body has to do work on the fluid.

Although it is often used as a simple explanation, added mass does not represent fluid that is rigidly bound to the wing by viscosity. It is an artefact of the fluid being given kinetic energy by the body. For that reason, since viscosity does affect the velocity of the fluid, it will affect the added mass, but is not necessary for the definition of added mass, see e.g. [38].

### 4.2 Potential form of added mass

The informal example of Section 4.1 is now revisited rigorously, using [39, pp. 94–95]. The kinetic energy can be expressed as:

$$T = \tfrac{1}{2} \int_V \rho \bar{u}_{\mathbf{T}}^2 \, dV, \tag{48}$$

where $V$ is the fluid volume. For the case of a thin, flat, two-dimensional plate, the above reduces to the familiar unsteady Bernoulli equation (10), e.g. [40, pp. 15–27], or [39, pp. 82–89]. The third term of (10) is the quasi-steady pressure, as used in Section 3. The first two terms relate to the added mass. However, since $p_0$ is constant, it can be ignored, so that the pressure due to added mass is:

$$p_{\mathrm{a}} = \rho \frac{\partial \Phi}{\partial t}. \tag{49}$$

The normal force for an upper or lower surface is obtained by integrating along the chord:

$$\begin{aligned} F_{\mathrm{NA}} &= -b \int_{-1}^{1} p_{\mathrm{a}} \, d\zeta \\ &= -\rho b \frac{\partial}{\partial t} \int_{-1}^{1} \Phi \, d\zeta, \end{aligned} \tag{50}$$

where the last step can be taken because the variable of the differentiation, $t$, is independent of the variable of integration $\zeta$, and $\Phi$ is continuously differentiable on $(-1, 1)$.

For the force normal to the wing, the difference $\Delta\Phi = \Phi^+ - \Phi^-$ in potential across the wing is considered. This gives the force:

$$F_{\mathrm{NA}} = -\rho b \frac{\partial}{\partial t} \int_{-1}^{1} \Delta\Phi \, d\zeta. \tag{51}$$

Because $\Phi$ has been defined in terms of the velocity of the fluid relative to the wing, but added mass is based on the velocity of the body relative to the fluid, the sign of $\Phi$ in eqn (51) has to be *reversed*:

$$F_{\mathrm{NA}} = +\rho b \frac{\partial}{\partial t} \int_{-1}^{1} \Delta\Phi \, d\zeta. \tag{52}$$

### 4.3 Total circulation

Integration of the potential in eqn (52) is not straightforward, because $\Phi$ is discontinuous at the leading edge. Instead, the standard method of thin aerofoil theory is employed, to form the total circulation along the upper surface of the wing from the leading edge to a point $\zeta$:

$$\Gamma^+(\zeta) = \int_{-1}^{\zeta} \gamma^+ \, d\zeta, \tag{53}$$

remembering that $\Gamma(-1) = 0$.

Now consider the integral of $\Phi$ from the trailing edge:

$$\Phi^+(\zeta) = \int_{1}^{\zeta} \gamma^+ d\zeta = \Gamma^+(\zeta) - \Gamma^+(1), \tag{54}$$

noting that $\Phi(1) = 0$. This means that the total circulation $\Gamma = \Gamma^+ + \Gamma^- = 2\Gamma^+$ can be substituted for $\Delta\Phi$ in eqn (52). This allows integration from the leading edge, since $\Gamma$ is 0 there, and therefore continuous. This method is similar to that of [33, p. 73]. This could also have been done by using $\Delta\Phi$ and integrating from the trailing edge: this was the method adopted by [35], but is more cumbersome. In either case, this is still a calculation based on potential. The potential is simply being expressed in terms of the bound vorticity of the wing, in accordance with thin aerofoil theory.

For the four given components of the potential, the equivalent total vorticity $\Gamma$ is found by integrating the vorticity $\gamma$, of eqns (4), (5), (8) and (9):

$$\Gamma_{\mathrm{TD}} = 2u_{\mathrm{N}} b Q \tag{55}$$

$$\Gamma_{\mathrm{RD}} = 2\dot{\beta} b^2 \left( \frac{\zeta Q}{2} - aQ \right) \tag{56}$$

$$\Gamma_{\mathrm{TK}} = 2u_{\mathrm{N}} b \left( a \, \sin(\zeta) + \pi/2 \right) \tag{57}$$

$$\Gamma_{\mathrm{RK}} = 2\dot{\beta} b^2 \left( \tfrac{1}{2} - a \right) \left( a \sin(\zeta) + \pi/2 \right) \tag{58}$$

Note the similarity of these expressions to those of the potential of eqns (2), (3), (6) and (7). The first two terms are identical, while the second two only differ by a constant $\pi$, to ensure that $\Gamma$ is zero at the leading edge, while $\Phi$ is zero at the trailing edge.

### 4.4 Accelerations

In order to find the acceleration, $u_{\mathrm{N}}$ is written in terms of the global velocities:

$$u_{\mathrm{N}} = u_{\mathrm{H}}\mathbf{S} + u_{\mathrm{V}}\mathbf{C}, \tag{59}$$

$$u_{\mathrm{Nm}} = u_{\mathrm{H}}\mathbf{S} + u_{\mathrm{V}}\mathbf{C} - \dot{\beta}ba, \tag{60}$$

$$u_{\mathrm{Nm}} = u_{\mathrm{H}}\mathbf{S} + u_{\mathrm{V}}\mathbf{C} + \dot{\beta}b\left(\tfrac{1}{2} - a\right). \tag{61}$$

This gives the accelerations:

$$\dot{u}_{\mathrm{N}} = \dot{u}_{\mathrm{H}}\mathbf{S} + \dot{u}_{\mathrm{V}}\mathbf{C} + 2\dot{\beta}u_{\mathrm{P}}, \tag{62}$$

$$\dot{u}_{\mathrm{Nm}} = \dot{u}_{\mathrm{H}}\mathbf{S} + \dot{u}_{\mathrm{V}}\mathbf{C} + 2\dot{\beta}u_{\mathrm{P}} - \ddot{\beta}ba, \tag{63}$$

$$\dot{u}_{\mathrm{Nr}} = \dot{u}_{\mathrm{H}}\mathbf{S} + \dot{u}_{\mathrm{V}}\mathbf{C} + 2\dot{\beta}u_{\mathrm{P}} + \ddot{\beta}b\left(\tfrac{1}{2} - a\right). \tag{64}$$

### 4.5 Normal added mass forces

Equation (52) is evaluated for the four components:

TD part:

$$\begin{aligned} F_{\mathrm{NA}} &= \rho b\frac{\partial}{\partial t}\int_{-1}^{1}\Gamma_{\mathrm{TD}}\,d\zeta \\ &= 2\rho b^2\frac{\partial}{\partial t}\left(u_{\mathrm{N}}\int_{-1}^{1}Q\,d\zeta\right) \\ &= \pi\rho b^2\dot{u}_{\mathrm{N}}. \end{aligned} \tag{65}$$

RD part:

$$\begin{aligned} F_{\mathrm{NA}} &= \rho b\frac{\partial}{\partial t}\int_{-1}^{1}\Gamma_{\mathrm{RD}}\,d\zeta \\ &= 2\rho b^3\frac{\partial}{\partial t}\dot{\beta}\int_{-1}^{1}\left(\frac{\zeta Q}{2} - aQ\right)d\zeta \\ &= -\pi\rho b^3 a\ddot{\beta}. \end{aligned} \tag{66}$$

The two Dirichlet components combine to give

$$F_{\mathrm{NAD}} = \pi\rho b^2\dot{u}_{\mathrm{Nm}}, \tag{67}$$

where $\dot{u}_{\mathrm{Nm}}$ is the normal acceleration of the midpoint of the wing.

TK part:

$$\begin{aligned} F_{\mathrm{NA}} &= \rho b\frac{\partial}{\partial t}\int_{-1}^{1}\Gamma_{\mathrm{TK}}\,d\zeta \\ &= 2\rho b^2\frac{\partial}{\partial t}\left(u_{\mathrm{N}}\int_{-1}^{1}\left(a\,\sin(\zeta) + \pi/2\right)d\zeta\right) \\ &= 2\pi\rho b^2\dot{u}_{\mathrm{N}}. \end{aligned} \tag{68}$$

RK part:

$$\begin{aligned} F_{\mathrm{NA}} &= \rho b \frac{\partial}{\partial t} \int_{-1}^{1} \Gamma_{\mathrm{RK}}\, d\zeta \\ &= 2\rho b^3 \left(\tfrac{1}{2} - a\right) \frac{\partial}{\partial t} \left( \dot{\beta} \int_{-1}^{1} \left(a \sin(\zeta) + \pi/2\right) d\zeta \right) \\ &= 2\pi\rho b^3 \left(\tfrac{1}{2} - a\right) \ddot{\beta}. \end{aligned} \tag{69}$$

The two Kutta–Joukowski components combine to give:

$$F_{\mathrm{NAK}} = 2\pi\rho b^2 \dot{u}_{\mathrm{Nr}}, \tag{70}$$

where $\dot{u}_{\mathrm{Nr}}$ is the normal acceleration of the 3/4-chord point of the wing, also called the *rear neutral point*.

### 4.6 Parallel added mass forces

$F_{\mathrm{PA}}$, the parallel added mass force, is formed by substituting normal acceleration components for parallel ones, similar to the way velocities were substituted to find $F_{\mathrm{PQ}}$ in Section 3.5. However, this cannot be done by simply substituting the parallel acceleration. Some of the terms above are the result of an increase in $\Gamma$ with the normal velocity. Intuitively, it is obvious that the plate will have smaller added mass when accelerating along its length than when it is accelerating normal to the chord, simply because in the second case it is blocking the flow.

The actual values are taken from [40, p. 27, equation (4.17)]. Sedov writes the added mass forces on the wing in the absence of wake circulation as:

$$\begin{aligned} X &= \lambda_y \Omega V + \lambda_{y\omega} \Omega^2, \\ Y &= -\lambda_y \frac{dV}{dt} - \lambda_{y\omega} \frac{d\Omega}{dt}, \end{aligned} \tag{71}$$

where $X, Y$ are the parallel and normal forces at the leading edge the velocities are $U, V$, and the rotational velocity is $\Omega$. $\lambda_y$ and $\lambda_{\omega y}$ are added mass coefficients, tabulated on p. 29 of the same reference: $\lambda_y = \rho\pi b^2$, $\lambda_{y\omega} = \rho\pi b^3$.

The expression for $X$ uses the same values of $\lambda$ as $Y$, so the expression for $X$ can be formed by making the following substitutions into the expression for $Y$:

$$\frac{dV}{dt} \;\rightarrow\; -\Omega V, \tag{72}$$

$$\frac{d\Omega}{dt} \;\rightarrow\; -\Omega^2. \tag{73}$$

From eqn (71), it can be seen that the expression for $Y$ is similar to the expression for normal force. By analogy with the above substitution, the substitution:

$$\dot{u}_{\mathrm{N}} \;\rightarrow\; -\dot{\beta} u_{\mathrm{N}} \tag{74}$$

$$\ddot{\beta} \;\rightarrow\; -\dot{\beta}^2 \tag{75}$$

is used in eqns (67) and (70) to yield:

$$\begin{aligned} F_{\mathrm{NAD}} &= \pi\rho b^2 \dot{u}_{\mathrm{Nm}} \\ &= \pi\rho b^2 \left(\dot{u}_{\mathrm{N}} - \ddot{\beta} b a\right) \\ F_{\mathrm{PAD}} &= \pi\rho b^2 \left(-\dot{\beta} u_{\mathrm{N}} + \dot{\beta}^2 b a\right) \end{aligned} \tag{76}$$

$$\begin{aligned} F_{\mathrm{NAK}} &= 2\pi\rho b^2 \dot{u}_{\mathrm{Nr}} \\ &= 2\pi\rho b^2 \left(\dot{u}_{\mathrm{N}} + \ddot{\beta} b \left(\tfrac{1}{2} - a\right)\right) \\ F_{\mathrm{PAK}} &= 2\pi\rho b^2 \left(-\dot{\beta} u_{\mathrm{N}} - \dot{\beta}^2 b \left(\tfrac{1}{2} - a\right)\right) \end{aligned} \tag{77}$$

### 4.7 Vertical and horizontal added mass forces

The normal and parallel forces are resolved into horizontal and vertical components:

$$\begin{aligned} F_{\mathrm{VAD}} &= F_{\mathrm{NAD}}\mathbf{C}_\beta + F_{\mathrm{PAD}}\mathbf{S}_\beta \\ &= \pi\rho b^2 \left[\dot{u}_{\mathrm{H}}\mathbf{S}_\beta\mathbf{C}_\beta + \dot{u}_{\mathrm{V}}\mathbf{C}_\beta^2 + 2\dot{\beta}u_{\mathrm{P}}\mathbf{C}_\beta - \ddot{\beta}ab\mathbf{C}_\beta - \dot{\beta}u_{\mathrm{N}}\mathbf{S}_\beta + \dot{\beta}^2 ab\mathbf{S}_\beta\right] \\ &= \pi\rho b^2 \left[\dot{u}_{\mathrm{H}}\mathbf{S}_\beta\mathbf{C}_\beta + \dot{u}_{\mathrm{V}}\mathbf{C}_\beta^2 + \dot{\beta}(2u_{\mathrm{P}}\mathbf{C}_\beta - u_{\mathrm{N}}\mathbf{S}_\beta) - \ddot{\beta}ab\mathbf{C}_\beta + \dot{\beta}^2 ab\mathbf{S}_\beta\right], \end{aligned} \tag{78}$$

$$\begin{aligned} F_{\mathrm{HAD}} &= -F_{\mathrm{NAD}}\mathbf{S}_\beta + F_{\mathrm{PAD}}\mathbf{C}_\beta \\ &= \pi\rho b^2 \left[-\dot{u}_{\mathrm{H}}\mathbf{S}_\beta^2 - \dot{u}_{\mathrm{V}}\mathbf{S}_\beta\mathbf{C}_\beta - 2\dot{\beta}u_{\mathrm{P}}\mathbf{S}_\beta + \ddot{\beta}ab\mathbf{S}_\beta - \dot{\beta}u_{\mathrm{N}}\mathbf{C}_\beta + \dot{\beta}^2 ab\mathbf{C}_\beta\right], \end{aligned} \tag{79}$$

$$\begin{aligned} F_{\mathrm{VAK}} &= F_{\mathrm{NAK}}\mathbf{C}_\beta + F_{\mathrm{PAK}}\mathbf{S}_\beta \\ &= 2\pi\rho b^2 \left[\dot{u}_{\mathrm{H}}\mathbf{S}_\beta\mathbf{C}_\beta + \dot{u}_{\mathrm{V}}\mathbf{C}_\beta^2 + 2\dot{\beta}u_{\mathrm{P}}\mathbf{C}_\beta - \ddot{\beta}b(a - \tfrac{1}{2})\mathbf{C}_\beta \right. \\ &\quad \left. -\dot{\beta}u_{\mathrm{N}}\mathbf{S}_\beta + \dot{\beta}^2(a - \tfrac{1}{2})b\mathbf{S}_\beta\right], \end{aligned} \tag{80}$$

$$\begin{aligned} F_{\mathrm{HAK}} &= -F_{\mathrm{NAK}}\mathbf{S}_\beta + F_{\mathrm{PAK}}\mathbf{C}_\beta \\ &= 2\pi\rho b^2 \left[-\dot{u}_{\mathrm{H}}\mathbf{S}_\beta^2 - \dot{u}_{\mathrm{V}}\mathbf{S}_\beta\mathbf{C}_\beta - 2\dot{\beta}u_{\mathrm{P}}\mathbf{S}_\beta + \ddot{\beta}b(a - \tfrac{1}{2})\mathbf{S}_\beta \right. \\ &\quad \left. -\dot{\beta}u_{\mathrm{N}}\mathbf{C}_\beta + \dot{\beta}^2 b(a - \tfrac{1}{2})\mathbf{C}_\beta\right]. \end{aligned} \tag{81}$$

### 4.8 Moments

The root moment of the wing is formed similarly to the quasi-steady case in Section 3:

$$M_{\mathrm{VA}} = RF_{\mathrm{VA}}r, \tag{82}$$

$$M_{\mathrm{HA}} = RF_{\mathrm{HA}}r. \tag{83}$$

Similarly, the pitching moment about the hinge is formed by revisiting the normal force expressions in eqns (67) and (70), and multiplying by the backwards offset from the hinge $b(a-\zeta)$.

Thus, the pitching moment becomes:

$$M_{\beta \mathrm{A}} = \rho b \frac{\partial}{\partial t} \int_{-1}^{1} \Gamma b \, (a - \zeta) \, . \tag{84}$$

The contributions for the four components, as for the forces, are:

TD part:

$$\Gamma_{\mathrm{TD}} = 2 u_{\mathrm{N}} b Q \tag{85}$$

$$\begin{aligned} M_{\beta \mathrm{ATD}} &= \rho b \frac{\partial}{\partial t} \int_{-1}^{1} \Gamma_{\mathrm{TD}} b \, (a - \zeta) \\ &= \pi \rho b^3 \dot{u}_{\mathrm{N}} a. \end{aligned} \tag{86}$$

RD part:

$$\Gamma_{\mathrm{RD}} = 2 \dot{\beta} b^2 Q \left( \tfrac{1}{2} \zeta - a \right) \tag{87}$$

$$\begin{aligned} M_{\beta \mathrm{ARD}} &= \rho b \frac{\partial}{\partial t} \int_{-1}^{1} \Gamma_{\mathrm{RD}} b \, (a - \zeta) \\ &= \pi \rho b^4 \ddot{\beta} \left( -a^2 - \frac{1}{8} \right) . \end{aligned} \tag{88}$$

TK part:

$$\Gamma_{\mathrm{TK}} = 2 u_{\mathrm{N}} b \big( a \sin (\zeta) + \pi / 2 \big) \tag{89}$$

$$\begin{aligned} M_{\beta \mathrm{ATK}} &= \rho b \frac{\partial}{\partial t} \int_{-1}^{1} \Gamma_{\mathrm{TK}} b \, (a - \zeta) \\ &= \pi \rho b^3 \dot{u}_{\mathrm{N}} \left( 2a - \tfrac{1}{2} \right) . \end{aligned} \tag{90}$$

RK part:

$$\Gamma_{\mathrm{RK}} = 2 \dot{\beta} b^2 \left( \tfrac{1}{2} - a \right) \big( a \sin (\zeta) + \pi / 2 \big) \tag{91}$$

$$\begin{aligned} M_{\beta \mathrm{ATK}} &= \rho b \frac{\partial}{\partial t} \int_{-1}^{1} \Gamma_{\mathrm{RK}} b \, (a - \zeta) \\ &= \pi \rho b^4 \ddot{\beta} \left( \tfrac{1}{2} - a \right) \left( a - \frac{1}{4} \right) . \end{aligned} \tag{92}$$

### 4.9 Comparison with standard results

Although the added mass force and moment expressions contain acceleration terms, they do not reduce to the acceleration at a single point. This is because the calculation of added mass entails all of the normal acceleration, but only some of the parallel acceleration.

If the Kutta–Joukowski term is removed, and $\beta = \dot{\beta} = \ddot{\beta} = 0$, then:

$$F_{\mathrm{NAD}} = F_{\mathrm{VAD}} = \pi\rho b^2 \left[\dot{u}_{\mathrm{V}} + 2\dot{\beta}u_{\mathrm{P}} - \ddot{\beta}ba\right] \tag{93}$$

$$= \pi\rho b^2 \dot{u}_{\mathrm{Vm}}. \tag{94}$$

This is the standard result of Jones, as outlined in [33, p. 192–194].

Another check is that for a closed cycle, $F_{\mathrm{VA}}$ and $F_{\mathrm{HA}}$ must sum to zero: they are *closed* functions. This does not apply to the forces $F_{\mathrm{NA}}$ and $F_{\mathrm{PA}}$, because they are defined relative to wing-fixed axes. The wing-fixed axes are not usable as inertial reference axes.

### 4.10 Wing integrals

The results above (which are forces per metre span) are converted to wing integrals, using the wing shape parameter method of Section 3.8. Again, it is assumed that the hinge is constant along the wing, which allows the use of a smaller set of wing shape parameters.

$$\begin{aligned} F_{\mathrm{VAD}} &= \pi\rho b^2 \left[\dot{u}_{\mathrm{H}}\mathbf{S}_\beta\mathbf{C}_\beta + \dot{u}_{\mathrm{V}}\mathbf{C}_\beta^2 + 2\dot{\beta}u_{\mathrm{P}}\mathbf{C}_\beta - \ddot{\beta}ab\mathbf{C}_\beta - \dot{\beta}u_{\mathrm{N}}\mathbf{S}_\beta + \dot{\beta}^2 ab\mathbf{S}_\beta\right] \\ F_{\mathrm{VADW}} &= \pi\rho RB^2 \left(\dot{u}_{\mathrm{HT}}\mathbf{S}_\beta\mathbf{C}_\beta + \dot{u}_{\mathrm{VT}}\mathbf{C}_\beta^2\right) b_2 r_1 + \pi\rho RB^2 \left(2\dot{\beta}u_{\mathrm{P}}\mathbf{C}_\beta - \beta u_{\mathrm{N}}\mathbf{S}_\beta\right) b_2 r_1 \\ &\quad + \pi\rho RB^3 \left(-\ddot{\beta}a\mathbf{C}_\beta + \dot{\beta}^2 a\mathbf{S}_\beta\right) b_3 r_0, \end{aligned} \tag{95}$$

$$\begin{aligned} F_{\mathrm{HAD}} &= \pi\rho b^2 \left[-\dot{u}_{\mathrm{H}}\mathbf{S}_\beta^2 - \dot{u}_{\mathrm{V}}\mathbf{S}_\beta\mathbf{C}_\beta - 2\dot{\beta}u_{\mathrm{P}}\mathbf{S}_\beta + \ddot{\beta}ab\mathbf{S}_\beta - \dot{\beta}u_{\mathrm{N}}\mathbf{C}_\beta + \dot{\beta}^2 ab\mathbf{C}_\beta\right] \\ F_{\mathrm{HADW}} &= \pi\rho B^2 \left(-\dot{u}_{\mathrm{H}}\mathbf{S}_\beta^2 - \dot{u}_{\mathrm{V}}\mathbf{S}_\beta\mathbf{C}_\beta\right) b_2 r_1 + \pi\rho B^2 \left(-2\dot{\beta}u_{\mathrm{P}}\mathbf{S}_\beta - \dot{\beta}u_{\mathrm{N}}\mathbf{C}_\beta\right) b_2 r_1 \\ &\quad + \pi\rho B^3 \left(+\ddot{\beta}ab\mathbf{S}_\beta + \dot{\beta}^2 ab\mathbf{C}_\beta\right) b_3 r_0, \end{aligned} \tag{96}$$

$$\begin{aligned} F_{\mathrm{VAK}} &= 2\pi\rho b^2 \left[\dot{u}_{\mathrm{H}}\mathbf{S}_\beta\mathbf{C}_\beta + \dot{u}_{\mathrm{V}}\mathbf{C}_\beta^2 + 2\dot{\beta}u_{\mathrm{P}}\mathbf{C}_\beta - \ddot{\beta}b(a - \tfrac{1}{2})\mathbf{C}_\beta \right. \\ &\quad \left. -\dot{\beta}u_{\mathrm{N}}\mathbf{S}_\beta + \dot{\beta}^2(a - \tfrac{1}{2})b\mathbf{S}_\beta\right] \\ F_{\mathrm{VAKW}} &= 2\pi\rho B^2 \left(\dot{u}_{\mathrm{H}}\mathbf{S}_\beta\mathbf{C}_\beta + \dot{u}_{\mathrm{V}}\mathbf{C}_\beta^2\right) b_2 r_1 + 2\pi\rho B^2 \left(+2\dot{\beta}u_{\mathrm{P}}\mathbf{C}_\beta - \dot{\beta}u_{\mathrm{N}}\mathbf{S}_\beta\right) b_2 r_1 \\ &\quad + 2\pi\rho B^3 \left(a - \tfrac{1}{2}\right) \left(-\ddot{\beta}\mathbf{C}_\beta + \dot{\beta}^2\mathbf{S}_\beta\right) b_3 r_0, \end{aligned} \tag{97}$$

$$\begin{aligned} F_{\mathrm{HAK}} &= 2\pi\rho b^2 \left[-\dot{u}_{\mathrm{H}}\mathbf{S}_\beta^2 - \dot{u}_{\mathrm{V}}\mathbf{S}_\beta\mathbf{C}_\beta - 2\dot{\beta}u_{\mathrm{P}}\mathbf{S}_\beta + \ddot{\beta}b(a - \tfrac{1}{2})\mathbf{S}_\beta \right. \\ &\quad \left. -\dot{\beta}u_{\mathrm{N}}\mathbf{C}_\beta + \dot{\beta}^2 b(a - \tfrac{1}{2})\mathbf{C}_\beta\right], \\ F_{\mathrm{HAKW}} &= 2\pi\rho B^2 \left(-\dot{u}_{\mathrm{H}}\mathbf{S}_\beta^2 - \dot{u}_{\mathrm{V}}\mathbf{S}_\beta\mathbf{C}_\beta\right) b_2 r_1 \\ &= 2\pi\rho B^3 \left(a - \tfrac{1}{2}\right) \left(+\ddot{\beta}b\mathbf{S}_\beta + \dot{\beta}^2 b\mathbf{C}_\beta\right) b_3 r_0. \end{aligned} \tag{98}$$

## 5 Polhamus leading edge and tip suction correction

### 5.1 Polhamus's analogy

In the context of sharp-edged delta wings the leading edge vortex was modelled by [24] who assumed that the separation at the leading edge is a 'hard' separation, causing total loss of leading edge suction, while the leading edge vortex causes a normal force component of equal magnitude. Effectively, the leading edge suction force is rotated by 90° onto the low-pressure side of the wing, as illustrated in Fig. 3. This is called the Polhamus leading edge suction analogy. Although this is a simple model, it has been shown to give remarkably good results, for example, in predicting the attached vortex lift of delta wings, see e.g. [41].

The Polhamus analogy is desirable for three reasons:

1. It is simple to implement.
2. It is compatible with inviscid potential flow theory.
3. It is easy to extend to complex wing geometries (see Section 5.2).

### 5.2 Correction for leading edge sweep

The leading edge suction of a two-dimensional wing section is called the leading edge thrust, since it is in the chordwise direction. For a swept wing, the leading edge suction force will actually be normal to the leading edge, but will still have the same forward thrust component. This means for a swept wing, the leading edge suction will be higher. It is the leading edge suction, not thrust that is rotated in the Polhamus approach. This is described in [42], who outline a correction to the Polhamus analogy for leading edges that are swept. It relies on the original Polhamus analogy for swept, sharp-tipped wings, and the extension of this theory to rectangular wings by Lamar, which is explained in [41]. The latter theory uses the Polhamus analogy on the tip suction force, causing an additional normal force component. The scheme of [42] uses these two theories to calculate the vortex lift for an arbitrary wing shape, as the summation of a series of trapezoidal wing sections.

For the flapping wing considered here, it is assumed the wing comes smoothly to a point at the tip. Because of this, there is no side edge to the wing, and therefore no tip suction, and no need for the Lamar extension described above.

### 5.3 Implementation

The method outlined in the previous section is used: at any given spanwise position, the leading edge thrust is expressed in terms of the quasi-steady force $F_{\mathrm{PQ}}$, given per unit span. Then the leading edge suction force $F_{\mathrm{S}}$, is found using the sweepback angle of the leading edge, $\angle$:

$$F_{\mathrm{S}} = F_{\mathrm{PQ}} / \cos(\angle), \tag{99}$$

where $\angle$ is defined as the angle between the leading edge and the outward (root to tip) direction, with $\angle$ positive when the leading edge is swept back. There is a potential numerical issue if very high resolution is used close to the leading edge, so that $\cos(\angle)$ may become close to 0. For this reason, and because it is easier to implement from $x, y$ coordinates of the wing geometry, we use the variable $\varphi$, which is equal to the rate of change of $x_1$ (the non-normalised chordwise

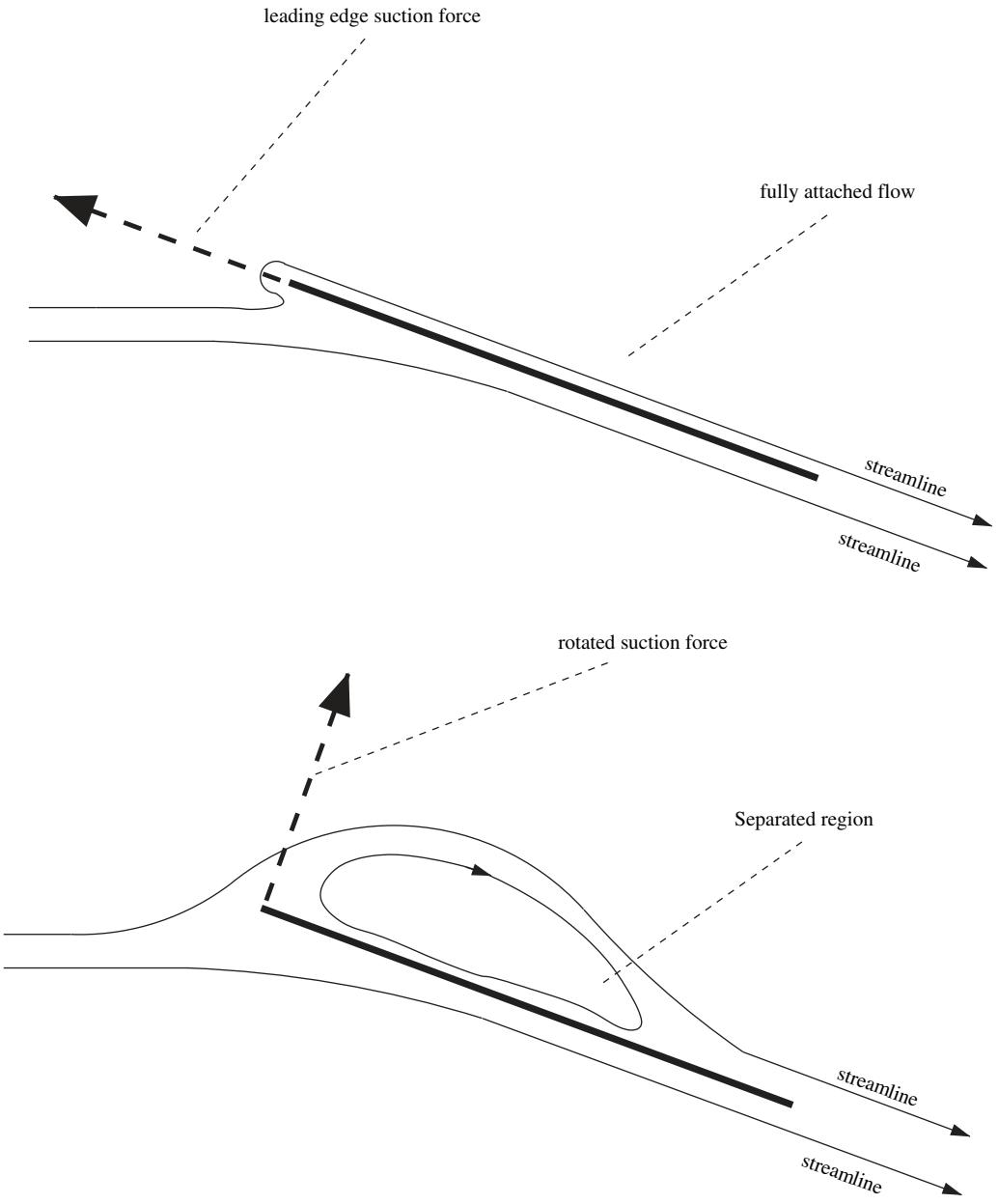


Figure 3: Illustration of the Polhamus leading edge suction analogy.

coordinate of the leading edge) with respect to the non-normalised radius. This yields:

$$F_S = F_{PQ}\sqrt{1+\varphi^2}. \tag{100}$$

### 5.4 Forces

The forces that result from the Polhamus effect are as follows:

$$F_{\mathrm{PP}} = -2\pi\rho b u_{\mathrm{Nr}} u_{\mathrm{Nm}} \tag{101}$$

$$F_{\mathrm{NP}} = 2\pi\rho b u_{\mathrm{Nr}} u_{\mathrm{Nm}} \sqrt{1+\varphi^2}\, T_{\mathrm{P}}. \tag{102}$$

The parallel component $F_{\mathrm{PP}}$ is simply the opposite of the leading edge thrust, calculated in Section 3. The normal force is this thrust force, scaled by $\sqrt{1+\varphi^2}$, to become the leading edge suction, as explained in Section 5.2. The parameter $T_{\mathrm{P}}$ is the sign of $u_{\mathrm{Nl}}$, the normal velocity at the leading edge, and determines on which side of the wing the leading edge suction occurs.

### 5.5 Wing integral

Similar to previous sections, the Polhamus forces on the entire wing are calculated by integrating along the wing. There is, however, one complication: since the semichord varies along the wing, the normal velocity at the leading edge will vary as well, and may reverse sign. This is dealt with by assuming that the turn direction is governed by the normal velocity at the leading edge at the point where the chord is maximum. Thus, the force on the entire wing due to the Polhamus effect is:

$$\begin{aligned} F_{\mathrm{PP}} &= -2\pi\rho b u_{\mathrm{Nr}} u_{\mathrm{Nm}} \\ &= -2\pi\rho b \left( u_{\mathrm{N}}^2 + u_{\mathrm{N}} \dot{\beta} b \left( \tfrac{1}{2} - 2a \right) + \dot{\beta}^2 b^2 \left( a^2 - a/2 \right) \right), \end{aligned} \tag{103}$$

$$\begin{aligned} F_{\mathrm{PPW}} &= -2\pi\rho BR\, u_{\mathrm{NT}}^2\, b_1 r_2 - 2\pi\rho B^2 R \dot{\beta} u_{\mathrm{NT}} \left( \tfrac{1}{2} - 2a \right) b_2 r_1 \\ &\quad - 2\pi\rho B^3 R \dot{\beta}^2 \left( a^2 - a/2 \right) b_3 r_0. \end{aligned} \tag{104}$$

Ignoring the turn direction and scaling above, the normal force is formed, assuming that the entire suction force is an upward normal force.

$$\begin{aligned} F_{\mathrm{NP}} &= 2\pi\rho b\, u_{\mathrm{Nr}} u_{\mathrm{Nm}} \sqrt{1+\varphi^2} \\ &= 2\pi\rho b \sqrt{1+\varphi^2} \left( u_{\mathrm{N}}^2 + u_{\mathrm{N}} \dot{\beta} b \left( \tfrac{1}{2} - 2a \right) + \dot{\beta}^2 b^2 \left( a^2 - a/2 \right) \right), \end{aligned} \tag{105}$$

$$\begin{aligned} F_{\mathrm{NPW}} &= -2\pi\rho BR\, u_{\mathrm{NT}}^2\, b_1 r_{2\mathrm{P}} - 2\pi\rho B^2 R \dot{\beta} u_{\mathrm{NT}} \left( \tfrac{1}{2} - 2a \right) b_2 r_{1\mathrm{P}} \\ &\quad - 2\pi\rho B^3 R \dot{\beta}^2 \left( a^2 - a/2 \right) b_3 r_{0\mathrm{P}}, \end{aligned} \tag{106}$$

where the wing shape parameters with subscript P are similar to the standard wing shape parameters, except they include the effect of leading edge sweep. For example:

$$b_2 r_1 = \int_{-1}^{1} \left( \frac{b}{B} \right)^2 r^1 \, dr \tag{107}$$

$$b_2 r_{1\mathrm{P}} = \int_{-1}^{1} \left( \frac{b}{B} \right)^2 r^1 \sqrt{1+\varphi^2} \, dr. \tag{108}$$

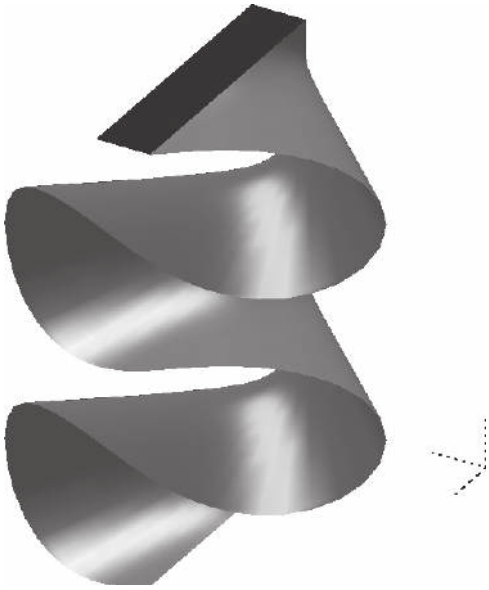

Figure 4: An example of a wake shape below a flapping wing, assuming uniform downwash velocity.

## 6 Wake effects

### 6.1 Potential form of wake model

The inviscid potential model of the wake is to treat it as a thin, continuous filament of vorticity being shed from the trailing edge of the wing, where any change in the bound circulation of the wing will cause an equal and opposite circulation to appear in the wake, to satisfy the Kelvin–Helmholtz theorem. In a real flow, the induced velocity due to the vorticity of the wing and wake will combine to cause motion and deformation of the wake filament. The presence of viscosity will introduce decaying effects into this process.

Assuming that the only motion of the wake is due to the uniform induced velocity $u_i$ (the downwash), a wake shape similar to that of Fig. 4 is obtained. However, in this model it is entirely possible for the wake to intersect with the wing, and for the wake to intersect itself.

The wake is by far the most complex part of the flow. In order to be able to isolate its effect in an analytically tractable way, simplifications have to be introduced. This simplification process is set in context by considering first exact solutions to simplified two-dimensional cases: the Wagner, Küssner and Loewy models.

### 6.2 Wagner's model

In his classical work Wagner [25] assumed the wing to be moving at a changeable forward velocity and angle of attack. The angle of attack was assumed small, and the velocity horizontal, so the wake filament becomes a straight horizontal line behind the wing. Wagner assumed this filament did not deform or move. Then he applied the quasi-steady force equations, similar to those in Section 3. However, the difference was that he integrated the effect of the entirety of the bound

vorticity and the shed vorticity, under the same assumption that there is no flow penetration on the wing. This reduced to a different expression for the bound vorticity, and hence lift, which was the original quasi-steady (wakeless) result plus a correction based on the effect of the wake. This was expressed as a function of the distance travelled in semichords measured since a given change in either angle of attack or forward velocity. From superposition, the change due to a time series of such changes can be expressed by simply summing the effect of every single change (using Duhamel's theorem, see e.g. [23]).

The Wagner function can be approximated by:

$$\psi'_{\mathrm{W}}(s) = 1 - 0.165e^{-0.041s} - 0.335e^{-0.32s}, \tag{109}$$

where $s$ is the semichord distance travelled by the aerofoil. Wagner's function expresses the delay between a step increase in the quasi-steady $C_{\mathrm{L}}$, till the wake-induced effects have decayed, and the full new lift coefficient is realised. It grows from $\frac{1}{2}$, meaning only half the lift from a step change is realised at once, and goes asymptotically to 1 as $s \to \infty$.

Using Duhamel's theorem, see [23] or [4], the effect of a series of step changes in $C_{\mathrm{L}}$ is:

$$C_{\mathrm{LW}}(s) = \int_{s_0}^{s_1} \frac{dC_{\mathrm{L}}(\sigma)}{d\sigma} \psi'_{\mathrm{W}}(s-\sigma)\, d\sigma, \tag{110}$$

where $C_{\mathrm{L}}$ is the wakeless (quasi-steady) lift coefficient, $C_{\mathrm{LW}}$ is the wake-modified coefficient, $\sigma$ is a dummy variable for integration, and the motion goes from position $s_0$ to $s_1$. It is assumed that no changes in $C_{\mathrm{L}}$ occurred before position $s_0$.

The perturbation Wagner function ($\psi_{\mathrm{W}}$) is defined as a perturbation from the quasi-steady lift *after* the step change. This is simply the expression of eqn (109) minus 1.

$$\begin{aligned} \psi_{\mathrm{W}}(s) &= \psi'_{\mathrm{W}}(s) - 1 \\ &= -0.165e^{-0.041s} - 0.335e^{-0.32s}. \end{aligned} \tag{111}$$

The perturbation form of the Wagner function in eqn (111) can serve as a correction to the wakeless quasi-steady result from Section 3. If the original Wagner function in eqn (109) were used, the quasi-steady component would be included twice: once in the quasi-steady calculation, and once in the non-perturbation form of the Wagner function.

The Duhamel sum of a series of changes in quasi-steady $C_{\mathrm{L}}$, using the perturbation Wagner function is:

$$C_{\mathrm{LW}} = \int_{s_0}^{s_1} \frac{dC_{\mathrm{L}}(\sigma)}{d\sigma} \psi_{\mathrm{W}}(s-\sigma)\, d\sigma. \tag{112}$$

This is the change in $C_{\mathrm{L}}$ due to the effect of the wake *only* ignoring the step change in $C_{\mathrm{L}}$ itself, which is already part of the quasi-steady solution. Again, it is assumed that no changes in $C_{\mathrm{L}}$ occurred before $s_0$.

### 6.3 Küssner's model

The Küssner wake model was introduced in [26], but that paper contained a sign error, which was corrected in [34]. The Küssner model is similar to the Wagner model, making the same assumptions about the wake being straight, horizontal and stationary in absolute space. However, instead of a change that applies to the entire wing at once, it considers a step increase in $C_{\mathrm{L}}$ that is

stationary in space. This could, for example, be a vertical gust region. The increase in $C_L$ does not apply everywhere along the wing, but propagates along it as the wing moves into the increased $C_L$ region. The Küssner function is also an expression based on $s$, and can be approximated by

$$\psi'_K(s) = 1 - \tfrac{1}{2}e^{-0.13s} - \tfrac{1}{2}e^{-s} \tag{113}$$

Küssner's function grows from 0, where the increased $C_L$ region is first encountered at the leading edge, but has not yet affected any of the wing, and goes asymptotically to 1 as $s \to \infty$ where the gust-disturbed flow is the new steady condition. Also note that the Küssner model includes the added mass effect, which the Wagner model does not.

Using Duhamel's theorem, see [23] or [4], the effect of a series of $C_L$ regions is:

$$C_{LK} = \int_{s_0}^{s_1} \frac{dC_L(\sigma)}{d\sigma} \psi'_K(s-\sigma)\, d\sigma, \tag{114}$$

where $C_L$ is the wakeless lift coefficient, $C_{LK}$ is the wake-modified coefficient, $\sigma$ is a dummy variable for integration and the motion goes from $s_0$ to $s_1$. It is assumed that no changes in $C_L$ occurred before $s_0$.

The perturbation Küssner function ($\psi_K$) is defined as a perturbation from the quasi-steady lift *after* the step change. This is simply the above expression minus 1.

$$\begin{aligned} \psi_K(s) &= \psi'_K(s) - 1 \\ &= -\tfrac{1}{2}e^{-0.13s} - \tfrac{1}{2}e^{-s}. \end{aligned} \tag{115}$$

The perturbation expression of eqn (115) can serve as a correction to the wakeless quasi-steady result. If the original expression of eqn (113) were used, the quasi-steady component would be included twice.

The Duhamel sum of a series of changes in $C_L$, using the perturbation Küssner function, is:

$$C_{LK} = \int_{s_0}^{s_1} \frac{dC_L(\sigma)}{d\sigma} \psi_K(s-\sigma)\, d\sigma. \tag{116}$$

This is the change in $C_L$ due to the effect of the wake *only* ignoring the step change in $C_L$ itself, which is already part of the quasi-steady solution. Again, it is assumed that no changes in $C_L$ occurred before $s_0$.

### 6.4 Loewy's model

The wake trailed behind the rotor of a hovering helicopter is convected downwards ('downwashed'). Due to the rotational motion, when the rotor returns to the same position in the rotation, it will pass over the wake it has shed earlier. Loewy [27] modelled this inviscidly by treating the wake as a straight horizontal vortex filament, as for the Wagner and Küssner models (see Fig. 5a–c). He assumed that the vorticity of the wing was varying sinusoidally, with spatial wavelength $\lambda$. He furthermore assumed that the helicopter had been in a steady hover for a long time, so the wake behind the rotor extended to infinity. This is the *primary* wake. The novelty of the Loewy approach was that he then modelled the encounter of previous wakes by reproducing the primary wake below the rotor, saying that during the cycle the wake would have moved downwards due to the uniform induced downwash $u_i$. He therefore modelled the wake passage as an infinite series of copies of the primary wakes (referred to here as secondary wakes), each offset by a constant distance down and advanced in phase by a constant number. This allowed him to obtain closed-form expressions for lift coefficients.

### 6.5 Modified Loewy model

Although the closed-form expressions of Loewy have not been employed here, his principle of secondary wakes has been utilised—treating the previous wakes as constantly offset straight vortex filaments below the wing. The difference is that computation is performed as a direct sum over the secondary wakes, rather than as closed-form expressions. The output of this model is the induced velocity at a point on the wing. Note that while Loewy's assumption that the distance between wakes is constant was justified in that the time between wakes is constant, in the case of flapping flight, the extreme ends of the stroke should actually meet to form a continuous filament. This is another simplification that was deemed necessary.

We now outline an adaptation of the Loewy approximation of helicopter wake effects, to flapping flight with stroke reversal.

Firstly, the nomenclature of [27] is collected:

- $n$ is the number of whole revolutions completed.
- $\gamma_a$ is the bound (attached) vorticity—this is called $\gamma_b$ in the following.
- $\gamma_{00}$ is the wake vorticity in the primary wake (behind the wing).
- $\gamma_{n0}$ is the wake vorticity in the secondary wakes (below the wing).
- $h$ is the vertical separation between full revolution blocks (from one $n$ to the next).
- $\Gamma_b$ is the total bound vorticity.

For the flapping-wing case Loewy's expression for induced velocity $u_w$ is:

$$u_{nw} = \frac{-1}{2\pi}\left[\int_{LE}^{TE} \frac{\gamma_a}{x-\zeta}\,d\zeta + \int_{TE}^{\infty} \frac{\gamma_{00}}{x-\zeta}\,d\zeta + \sum_{n=1}^{\infty}\int_{-\infty}^{\infty} \frac{\gamma_{n0}(x-\zeta)}{(x-\zeta)^2+n^2h^2}\,d\zeta\right]. \tag{117}$$

This is simply an expression of the two-dimensional Biot–Savart law for all the vortical elements. The first term is the bound vorticity, the second term is the primary wake vorticity, and the summation of the final term is all of the secondary wakes.

Next, Loewy used the reduced frequency to express the above spatial integrals in terms of time. This reduction cannot be used here, because the forward velocity of the flapping wing is not constant. However, the spatial distribution of the wake vorticity, in terms of the length travelled $s$, can be found and represented as a sum of sinusoidal elements using the fast Fourier transform. The induced velocity, caused by each sinusoidal element, can be calculated, and the vector sum of velocities formed to produce the total effect. In this way, the finite extent of the secondary wakes is taken into account directly, while the essence of Loewy's approach is preserved through the Fourier decomposition of the wake's vorticity.

### 6.6 Combined wake model

The models of Sections 6.2, 6.3 and 6.4 are combined to form a wake model of the actual, complex wake shape behind and below a flapping wing. Firstly, the wake is split into single-stroke segments, similarly to Loewy's model. The *primary* wake extends backwards in a horizontal line, to the start of the current stroke, and a number of *secondary* wakes, due to previous strokes, that are horizontal lines, each one offset by the distance $u_i T/2$ below the later stroke, where $u_i$ is the average downwash velocity, and $T$ is the period of a complete cycle, so $T/2$ is the period of a single stroke (see Fig. 5).

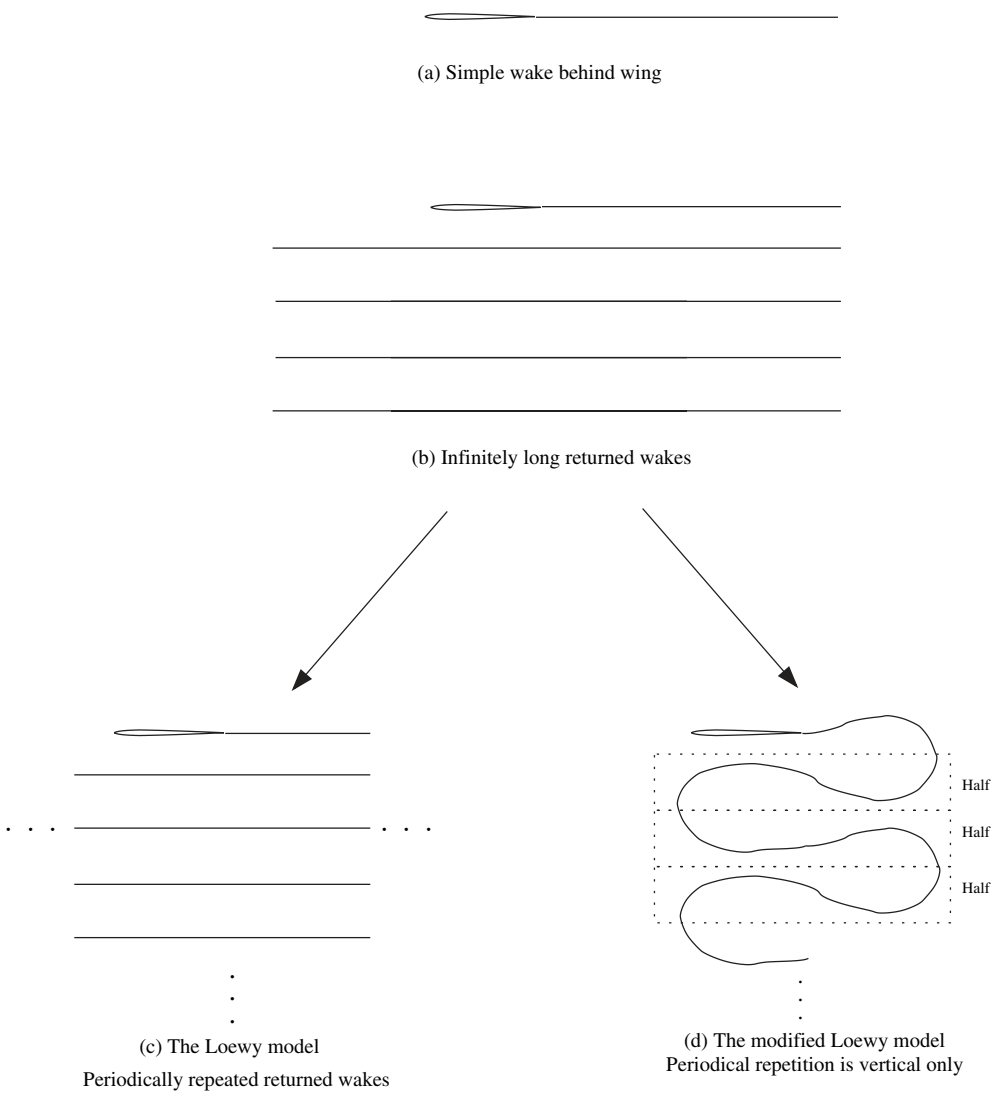


Figure 5: Illustration of the original and modified Loewy returning wake model.

The analysis is restricted to two-dimensional, assuming that the wing can be treated as a series of two-dimensional spanwise segments, that do not affect each other. Also, this assumes that there is no spanwise flow.

The start and the end of the stroke are governed by the position of the trailing edge, which is where the wake is being shed from.

The primary wake is assumed to be a line, so the effect of the primary wake can be treated as a Wagner-type effect, by applying the Wagner function to the changes in the quasi-steady lift coefficient $C_L$ since the start of the current stroke. It is assumed that the compounded effect of the Wagner contributions from previous strokes instantly disappear at the start of a new stroke. However, at the start any stroke after the first, only the change in $C_L$ between strokes is used—this is the step change in $C_L$ from the end of one stroke to the start of the next. If the entire $C_L$

was used to calculate the Wagner effect at the start of each stroke, the model would give us an unrealistically strong starting vortex, as if the wing had just impulsively started from rest at the start of the stroke.

The effect of the secondary wakes is incorporated by calculating the induced velocity at the leading edge, due to the vorticity of all the secondary wakes, in a Loewy-type sum. These secondary wakes are assumed to be straight lines, and globally stationary, so the flowfield they cause is also globally stationary. The velocities induced by the secondary flowfield are treated as stationary gusts, and their effect on the wing is modelled as a Küssner-type effect. This is done by calculating $C_L$ with and without the secondary wake-induced velocities, and treating the difference in $C_L$ as a series of Küssner perturbations. Again, to avoid the start of a stroke being modelled as if it were an impulsive start, $C_L$ at the start of the stroke is taken as the step change since the end of the previous stroke, similarly to the method used for the Wagner effect above.

The effects of the primary and secondary wakes are treated as entirely separate, but superposable.

### 6.7 Added mass and the wake

In our model, the added mass does not affect the wake. This is because:

- The added mass is a purely irrotational effect, and therefore will not affect the bound vorticity of the wing, or the vorticity in the wake.
- The wake is modelled as a prescribed shape (line segments), so the added mass cannot affect the shape of the wake.

Under these conditions, the added mass cannot affect the wake. However, as the wake affects the velocity of the fluid around the wing, it has an effect on the added mass. This has not been modelled accurately, because no Wagner-type function exists for this effect. The Küssner function already includes the effect of added mass.

### 6.8 Polhamus correction and the wake

It is expected that the leading edge vortex will cause a change in the bound vorticity and, therefore, wake vorticity. For usual cases, where the incoming velocity is approximately parallel to the chord, the increased normal force due to the rotation of the leading edge suction can be modelled by an increase in bound circulation of the wing. However, for flapping kinematics, the incoming velocity is not approximately parallel to the chord. Therefore, for our case we cannot use a vorticity model of the Polhamus correction, as mentioned in Section 5.

For this reason, the effect of the leading edge vortex on the wake cannot be modelled accurately. A simple correction for the effect of the leading edge vortex has been applied, by using the Polhamus-modified $C_L$ in the wake calculations.

Similarly, because the Wagner and Küssner functions treat the wing and wake as horizontal, they predict the force that results to be purely normal to the wing, so no parallel component exists. This means they do not have an effect on the leading edge suction. It is technically possible to derive expressions similar to Wagner and Küssner's function, but for the leading edge suction. However, if this is applied to the Polhamus effect, it leads to an iterative model, where the results of an earlier function are affected by the results of a later one.

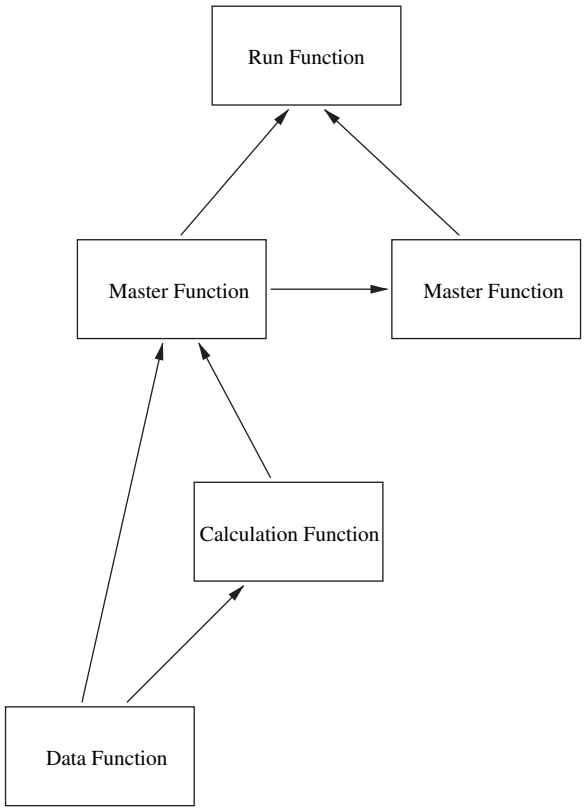


Figure 6: Code overview: The hierarchy of functions. Note that the flow of information is always upwards, or horizontal, never down, so that only non-iterative (one-pass) computation is involved.

## 7 Code implementation

The code was implemented in MATLAB because of the great deal of inbuilt functionality for handling vectors and matrices it offers, which made code development easier, but—more importantly—makes the code far more compact and legible.

The code was split into a number of functions. Because the theory devised is non-iterative, it was possible to arrange them hierarchically by type, as shown in Fig. 6. Briefly, the top-level, run functions are the command used to execute the entire code. These in turn call the master functions, which calculate the results for a given part of the model, e.g. the quasi-steady forces. They do this by calling calculation functions that deal with a specific aspect of the calculation. At the lowest level, the data functions provide all the data needed by the other functions. The flow of information in the figure is almost entirely upwards. The exception is the quasi-steady results from the quasi-steady master functions, which are used by other master functions. At no point does information flow down the hierarchy. As already stressed, an important feature of this model is that it is non-iterative, so the flow of information is unidirectional.

The code runs in less than five minutes on a 1.8 GHz Pentium IV computer.

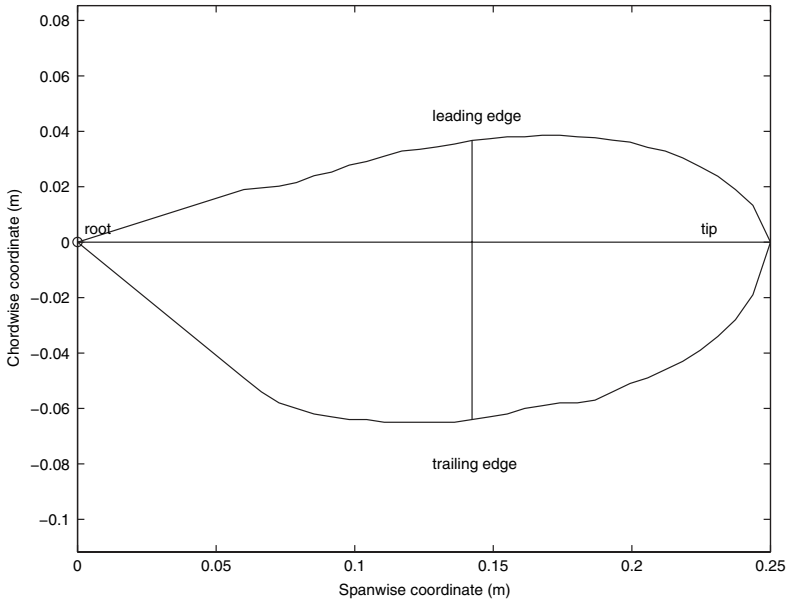


Figure 7: Robofly wing geometry. The horizontal and vertical lines are the hinge line (from the root to the point furthest from the root), and the maximum chord line (the longest line normal to the hinge line), respectively.

## 8 Dickinson's Robofly data

Dickinson's Robofly is a mechanical device that mimics the kinematics of a hovering insect, by controlling the movement of a wing at the root with electric motors. The wing is a scaled-up version of a fruit fly wing, which is flapped in mineral oil at low frequency, to preserve dynamic similarity with the original fruit fly. The frequency was 0.168 Hz, giving a period of about 6 s for a full cycle. The equipment and procedures are explained in [43–45]. The data provided were for the 'advanced' case of [43], where the wing rotation leads the wing reversal.

### 8.1 Geometry

The wing geometry of Dickinson's Robofly is a scaled version of a *Drosophila Melanogaster* fruit fly wing. The tip radius is 250 mm, but the inner 60 mm of the wing is taken up with sensors, and is assumed not to contribute to the force. The shape is shown in Fig. 7, where for the purpose of the plot the inner 60 mm of the wing has been shown with straight trailing and leading edges.

### 8.2 Kinematics

The Robofly kinematics follow a simplified pattern, see Fig. 8, and do not mimic those of any particular insect. The sweeping motion (change of $\theta$) is approximately a triangular wave, with near-constant sweeping velocity during midstroke. The sweeping amplitude is 80°, so the wing completes almost half a revolution each stroke. There is no plunging motion. The pitching is

approximately a square wave, with very sharp rotation—note that this is Dickinson's data for advanced rotation so the rotation occurs before the hinge point comes to a stop at the end of a stroke.

## 9 Indicial-Polhamus model prediction for Robofly data

### 9.1 The 'lift' force, $F_V$

The data comprise eight strokes, in four full cycles. The results are not exactly equal from one stroke to the next, most noticeably the first stroke has a very suppressed initial peak compared with the rest; this is consistent with the Wagner effect. The average lift is 0.40 N. These experimental data will be reproduced on the following plots as a dotted line, for comparison.

The following description will start with comparing the experimental results with the quasi-steady results, as shown in Fig. 9. Then, those results will be modified by adding the corrections for Polhamus, wake effects and added mass, one at a time. Finally, a modification of the added mass model that gives a better fit with the experimental results is suggested.

Referring to Fig. 9, which shows the predicted quasi-steady lift on the entire wing versus the measured lift, it can be seen that lift is almost constant during the translation at the middle of each stroke, followed by a very sharp peak and trough at the rotation. These peaks are almost entirely due to suction forces, and are much lower in the measured data. Also, the quasi-steady model overpredicts lift by approximately a factor of 2. Typically, quasi-steady models will underpredict flapping-wing aerodynamics, because they eliminate a number of rotational terms that a negligible in standard aerodynamic applications. By including these rotational terms in the derivation of the quasi-steady model in Section 3, we obtain results that more correctly model flapping-wing aerodynamics. Our quasi-steady model overpredicts the lift, because it does not yet include any of the loss-inducing effects such as wake influence.

Adding the Polhamus correction in Fig. 10 gives the Polhamus-corrected lift shown in Fig. 11, which fits the measured data better. It is seen that the lift peak in Fig. 9 is effectively cancelled by the Polhamus effect in Fig. 10. This is because the lift peak coincides with the wing being almost vertical, at which point lift is derived mainly from leading edge suction. The Polhamus effect rotates this suction force by 90°, and turns it into a horizontal force. Polhamus has very little effect on the lift during translation, because the wing is at 45°, so when the leading edge suction force is rotated by 90°, its vertical component is almost the same. The fact that it changes at all is because of the scaling due to leading edge sweep. The overall shape of the Polhamus-corrected lift in 11 is similar to that measured, but overpredicts lift by almost a factor of 2, and is missing some salient features of the shape. Again, this overprediction is because our model does not yet include loss-inducing wake effects.

Adding the primary wake correction for lift in Fig. 12, gives the Wagner-corrected lift in Fig. 13. The lift is now considerably reduced, and illustrates how the Wagner effect opposes increases in lift by reducing and delaying them. Note that the lift is now increasing during the translation, matching the experiment.

Adding the secondary wake lift correction in Fig. 14 gives the Küssner-corrected lift in Fig. 15. This correction acts mainly to reduce the lift at midstroke. It is zero during the first stroke, because there is no secondary wake until the first reversal. After that, it starts out strongly asymmetric due to the strong starting vortex and unbalanced secondary wakes, but tends to similarity between strokes as time progresses, as the starting vortex is further from the wing and the secondary wake tends to a long series of asymmetric wakes.

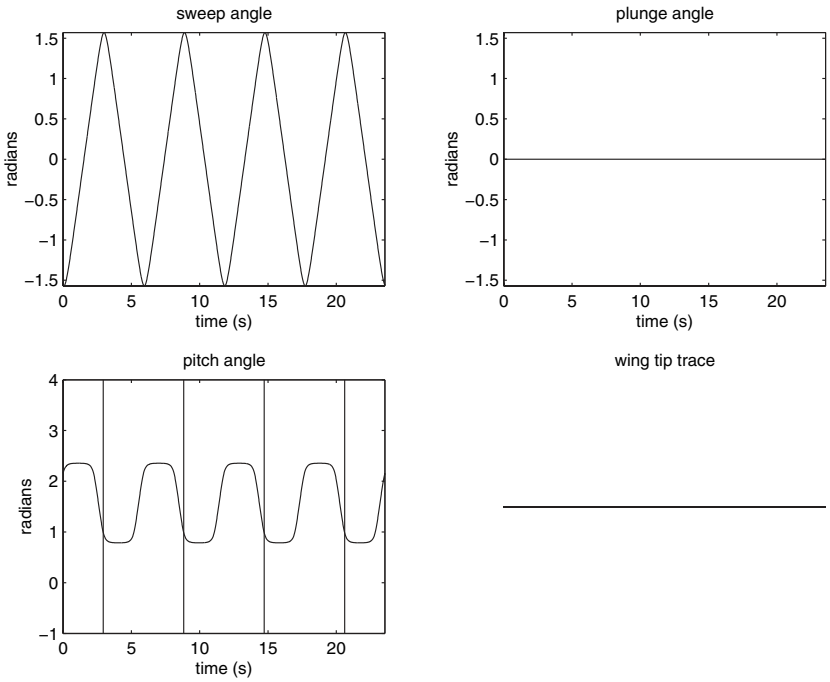


Figure 8: Robofly wing kinematics: the first stroke starts forwards (negative sweep angle $\theta$) with the wing past the vertical. Angles are given in radians.

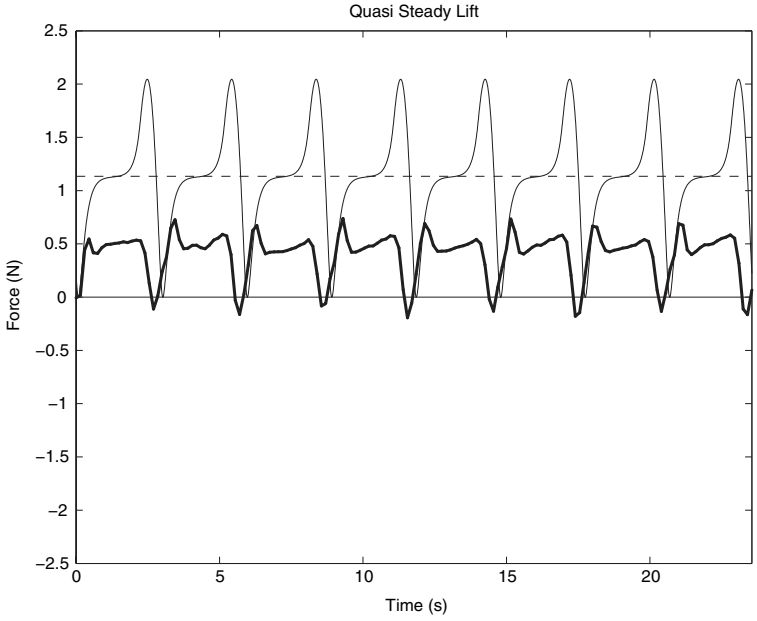


Figure 9: Predicted quasi-steady lift (thin line) versus measured Robofly lift (thick line); the dashed line is the average predicted force.

At this stage, one salient feature of the lift trace is not picked up—the upward 'bump' at the start and end of each translation phase. This is a compound effect of (a) ignoring added mass and (b) the simplified secondary wake. Because the modelled shape of the secondary wake has discrete 'jumps' at the end of every stroke, the effect is to under-predict the secondary wake effect at the start of every stroke.

Including the added mass effect in Fig. 16 gives the added-mass-corrected lift shown in Fig. 17, which highlights a major limitation of the model. Although the added mass does have the missing bumps, they are both far too large, and occur too soon to match those of the measured data. It is postulated that this is a direct effect of omitting the attenuating effect of the wake on the added mass, the effect of which would be to reduce, delay and smooth the added mass force. This postulation is outlined below.

It is worth noting that the added mass effect is the sum of two components: the irrotational Dirichlet solution, and the Kutta–Joukowski component, see eqns (67) and (70). If we add only the Dirichlet component of the added mass shown in Fig. 18 to the wake-corrected lift in Fig. 15, the final result become the Dirichlet-corrected lift shown in Fig. 19. It can be seen that the Dirichlet added mass corrections in Fig. 18 has the correct 'bumps', at what seems to be the correct magnitude, but they are occurring too soon.

Now consider if we add only the the Kutta–Joukowski part of the added mass in Fig. 20, to the wake-corrected lift in Fig. 15, the final result becomes the Kutta–Joukowski-corrected lift in Fig. 21. It can be seen that the Kutta–Joukowski added mass corrections in Fig. 20 has the correct 'bumps', that occur too soon much like the Dirichlet component above, but also the magnitude is far too large.

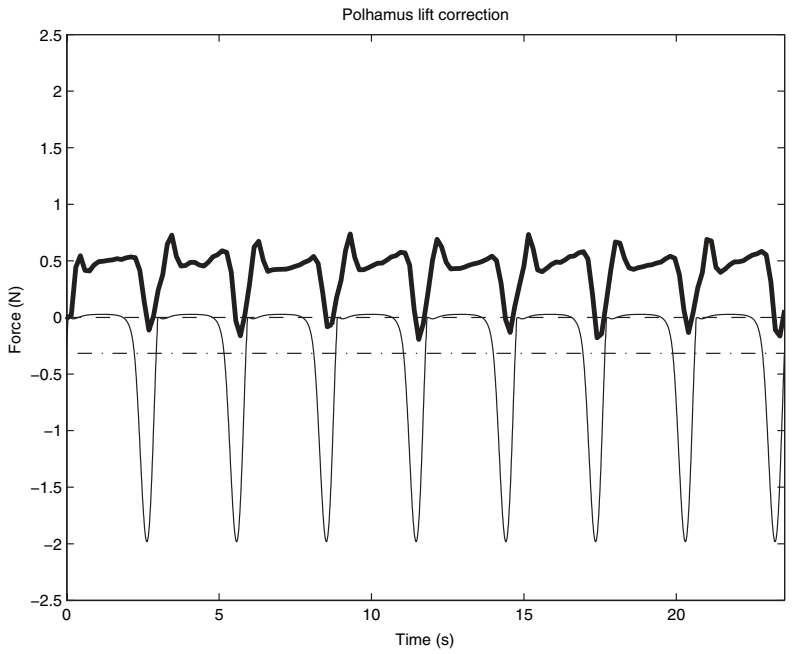


Figure 10: Polhamus correction to lift (thin line) versus measured Robofly lift (thick line); the dashed line is the average predicted force.

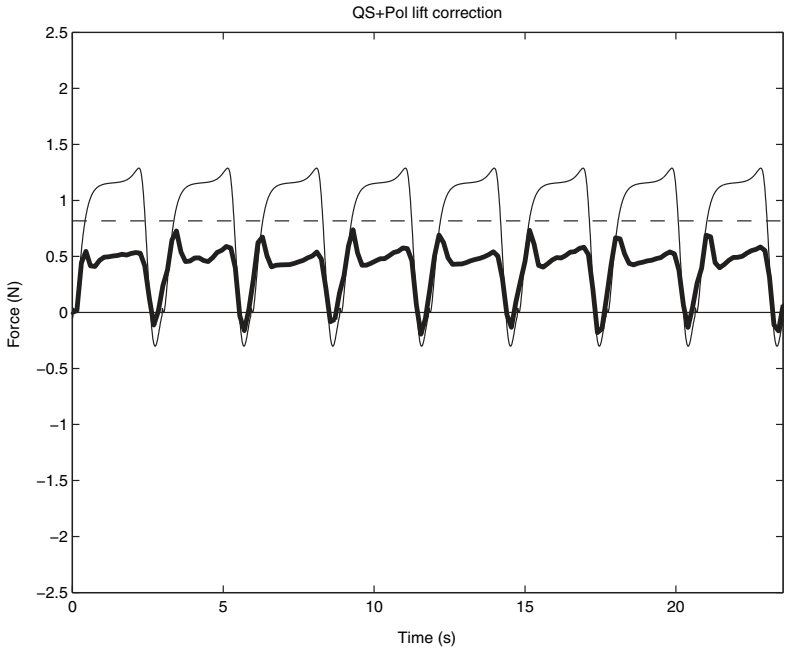


Figure 11: Quasi-steady lift modified by Polhamus correction (thin line) versus measured Robofly lift (thick line); the dashed line is the average predicted force.

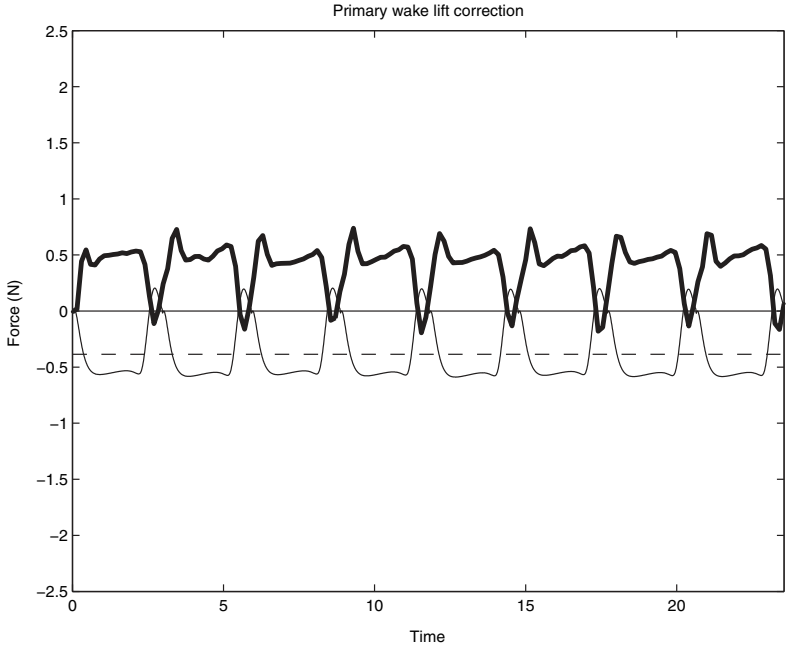


Figure 12: Wagner correction to lift (thin line) versus measured Robofly lift (thick line); the dashed line is the average predicted force.

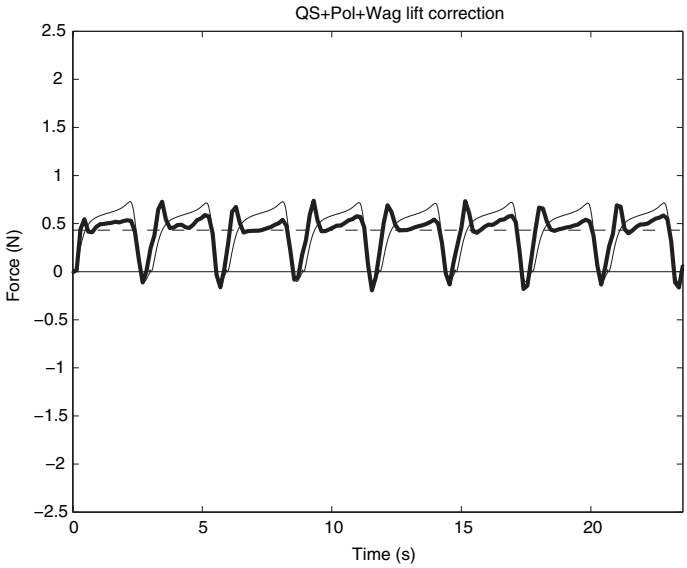


Figure 13: Quasi-steady lift modified by Polhamus and primary wake (Wagner) correction (thin line) versus measured Robofly lift (thick line); the dashed line is the average predicted force.

This comparison between the two components of the added mass leads to the conclusion that the main problem with the added mass model is that it is neglecting the attenuating effect of the wake on the added mass lift. This is justified partly by the added mass components occurring too soon, but mainly because the Kutta–Joukowski part of the added mass model is a worse fit than the Dirichlet part. This, in turn, we link to the fact that the Dirichlet part derives from an irrotational solution that requires no wake vorticity, while the Kutta–Joukowski component requires wake vorticity, and therefore the missing modelling of the attenuating wake effect on the added mass is more severe for the Kutta–Joukowski component.

This leads to an empirical correction to the added mass model, based loosely on the Wagner function: that the added mass includes the entirety of the Dirichlet part, but only half of the Kutta–Joukowski part, as shown in Fig. 22. This is a considerable improvement over the result in Fig. 17. There is no particular theoretical justification for choosing the factor $\frac{1}{2}$, except that the Wagner effect predicts the loss of half the circulatory quasi-steady lift, so it seemed a valid guess for the loss of circulatory added mass lift, too. A similar approach has been suggested by [46]. Note how well the scaled added mass figure matches the measured result, picking up all the critical features of the force trace, although they manifest a little too soon and with too much magnitude. This is especially true for the loss of lift at rotation, which is being heavily overpredicted. Again, this is because the rotation is associated with strong vortex shedding, the effect of which on the added mass are not modelled. This underlines the conclusion that the model captures the unsteady aerodynamics rather well, but lacks a critical component in the modelling of the wake effect on the added mass.

Figure 23 shows the result of Fig. 19, without correcting the force coefficients for the effect of Polhamus, i.e. setting the variable *usepolhamus* = *'no'* in the code. It shows that without the Polhamus correction to lift coefficients, the model heavily under-predicts $F_V$ during rotation, because it is compensating for suction lift that is not being realised.

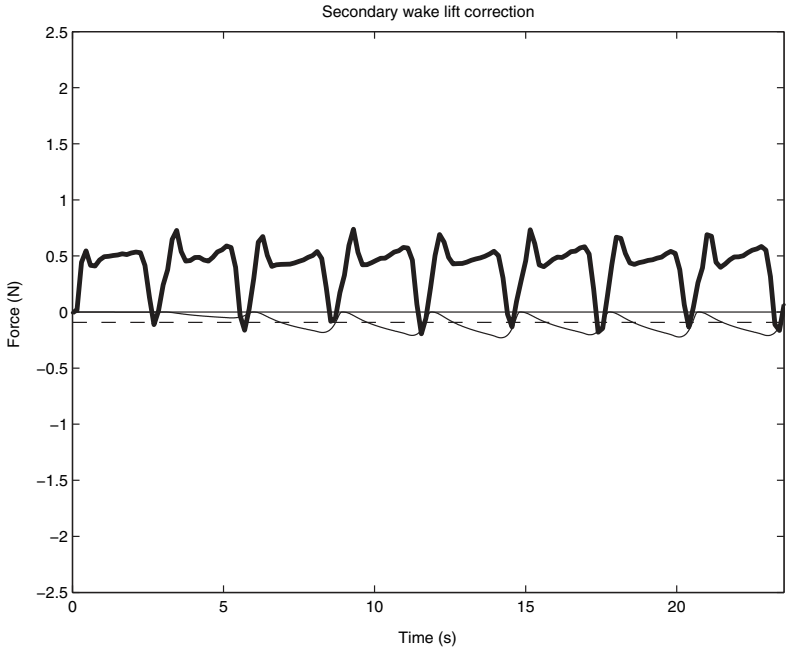


Figure 14: Secondary wake (Küssner) correction to lift (thin line) versus measured Robofly lift (thick line); the dashed line is the average predicted force.

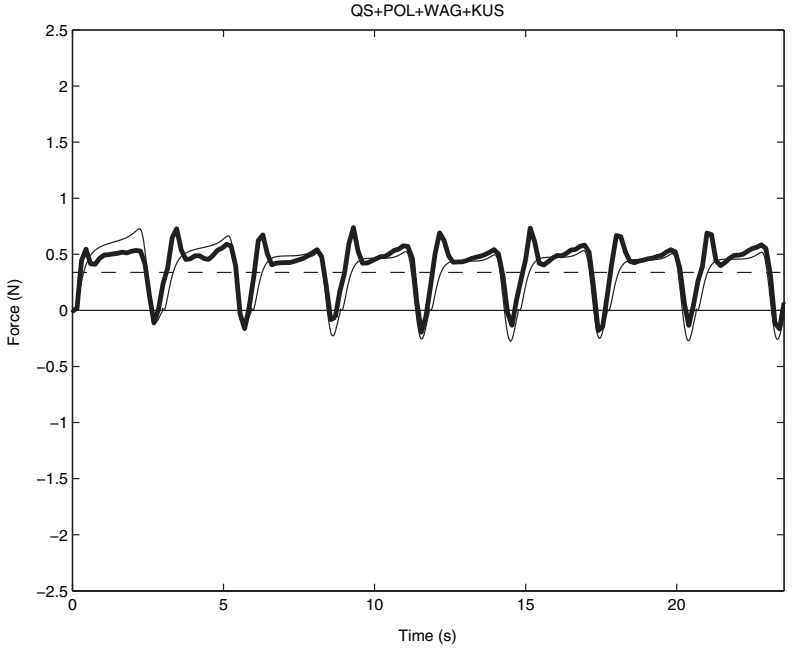


Figure 15: Quasi-steady + Polhamus + primary and secondary wake corrections to lift (thin line) versus measured Robofly lift (thick line); the dashed line is the average predicted force.

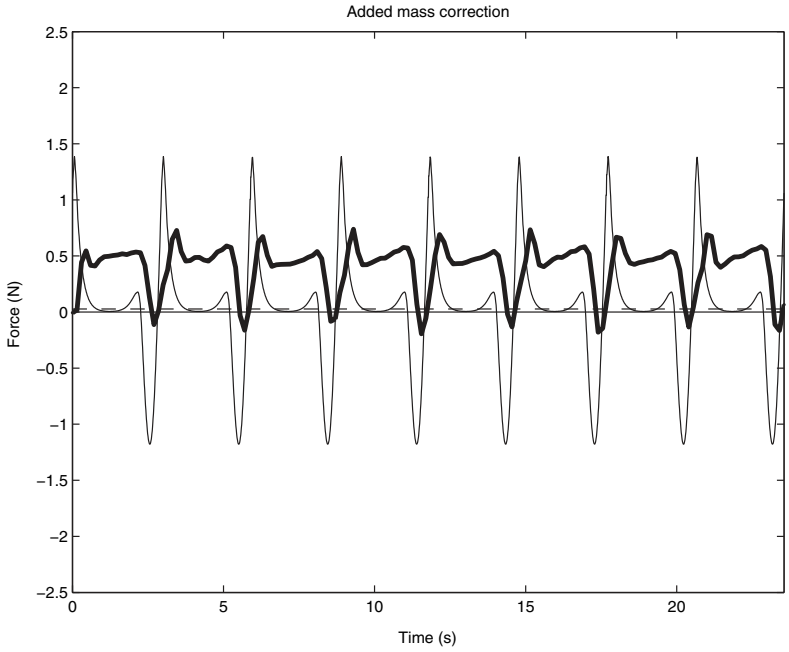


Figure 16: Added mass correction to lift (thin line) versus measured Robofly lift (thick line); the dashed line is the average predicted force.

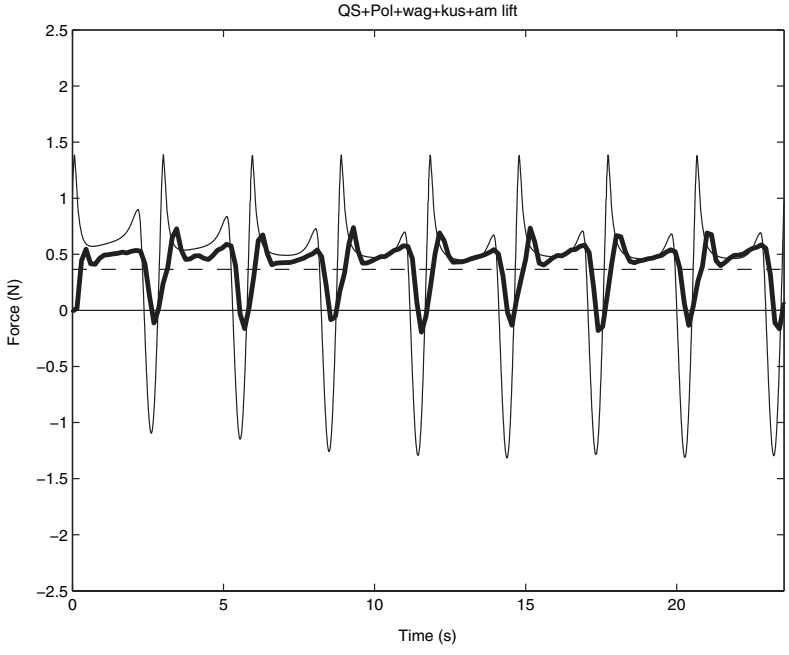


Figure 17: Total lift including added mass forces (thin line) versus measured Robofly lift (thick line); the dashed line is the average predicted force.

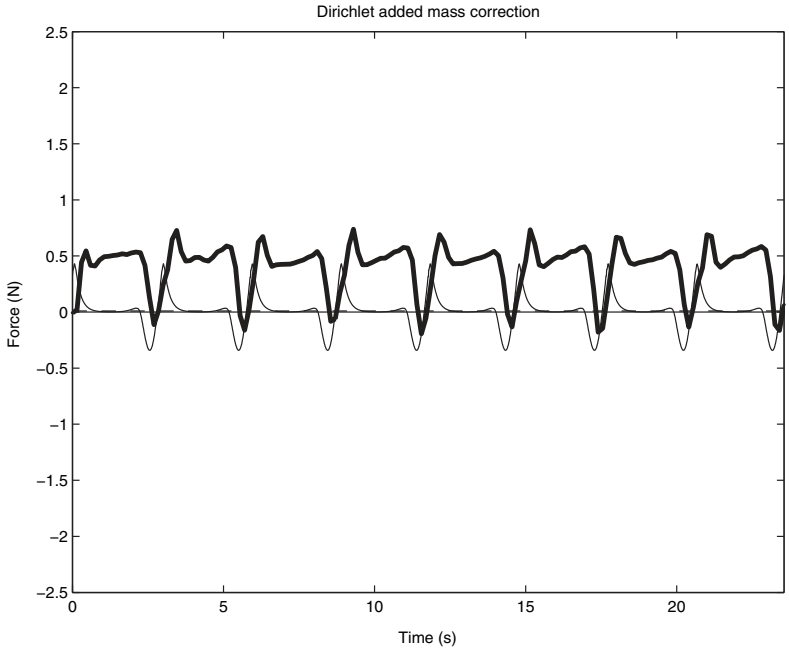


Figure 18: Dirichlet component of the added mass correction to lift (thin line) versus measured Robofly lift (thick line); the dashed line is the average predicted force.

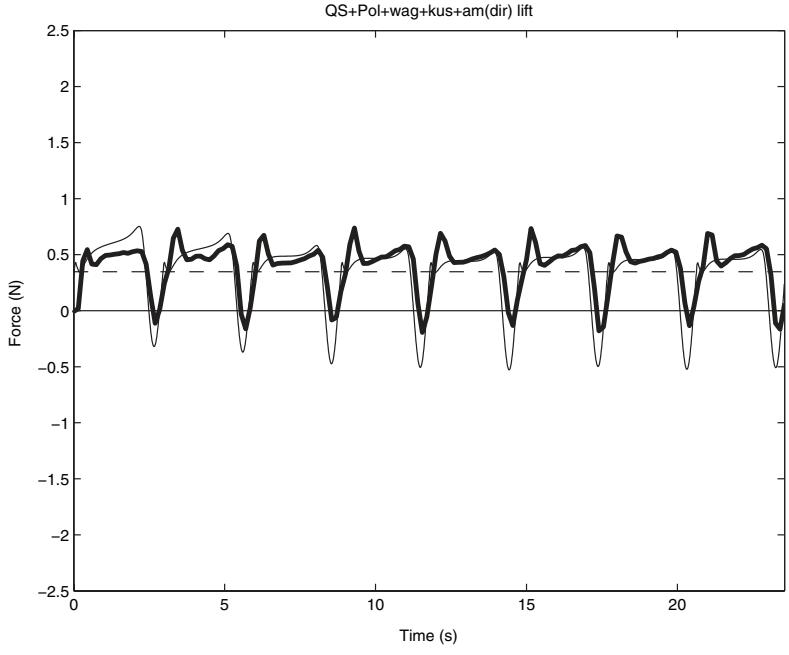


Figure 19: Total lift, including the Dirichlet component of added mass forces (thin line) versus measured Robofly lift (thick line); the dashed line is the average predicted force.

Added mass does not contribute a net force over a closed cycle—so the inaccuracy of the added mass effect above does not have an effect on the average lift. The average measured lift is 0.40 N, and the average predicted lift from the model is 0.37 N, a 7.8% error.

### 9.2 The 'drag' force

Dickinson defined drag in terms of the horizontal force in the direction opposing motion, therefore it was always positive. Our model defines horizontal force ($F_H$) in the $+\theta$ direction. Therefore, to compare with Dickinson's data, value of the predicted drag was multiplied by the sign of the horizontal tip velocity $u_{HT}$. Considering Fig. 24 it can be seen that there is almost no quasi-steady drag. This fits well with the theory, as there is very little vertical velocity of the midpoint. (There is no plunging motion, so the only vertical velocity is due to the rotation and the hinge offset from the midpoint, and the hinge is almost at the midpoint.)

The Polhamus effect is considerable, as seen in Fig. 25. Much like the quasi-steady lift force does, the Polhamus effect overpredicts the drag force by a factor of 2. This is because the Polhamus effect is a rotation of the quasi-steady suction force and therefore scales with the suction force. However, the model predicts very little effect of the wake on drag for the first component, because Wagner's function does not predict any effect due to the primary wake, and for the second part, because the secondary wake effect is small, just as it was for lift (see Fig. 26). Therefore only the Polhamus correction is left, which is considerable. The Polhamus correction did not affect lift during translation, but it has considerable effect on drag. Again, this is because when the leading edge suction (which is at 45°) is rotated, its vertical component is almost unchanged, but the horizontal component changes sign.

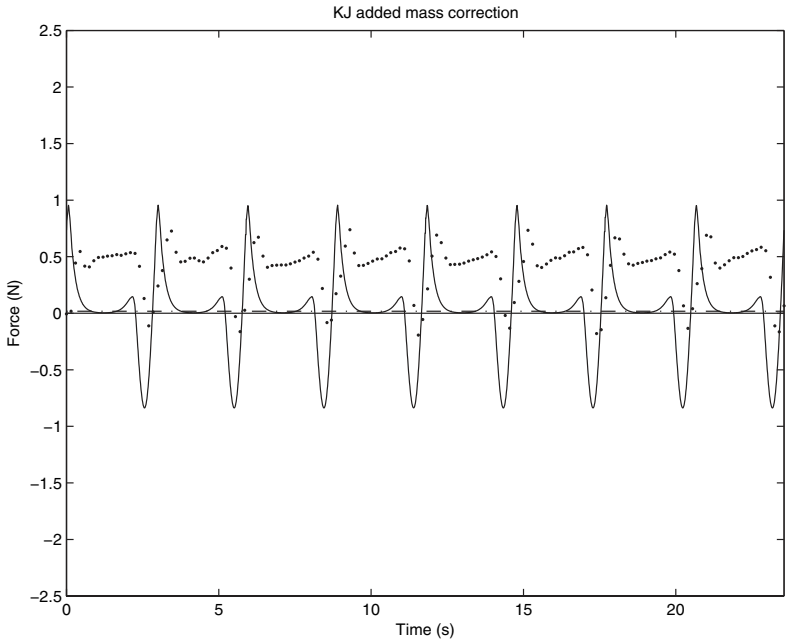


Figure 20: Kutta–Joukowski component of the added mass correction to lift (thin line) versus measured Robofly lift (dotted line); the dashed line is the average predicted force.

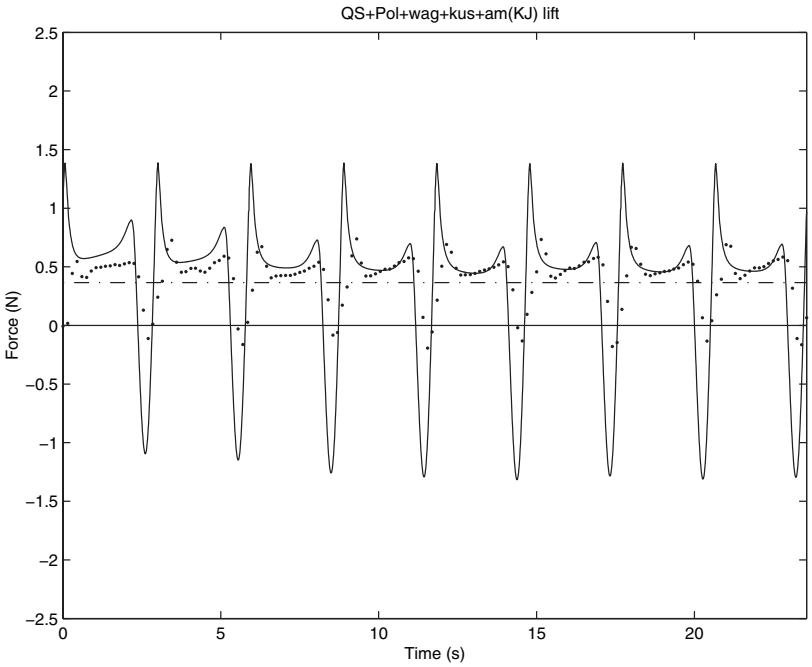


Figure 21: Total lift, including the Kutta–Jokowski component of added mass forces (thin line) versus measured Robofly lift (dotted line); the dashed line is the average predicted force.

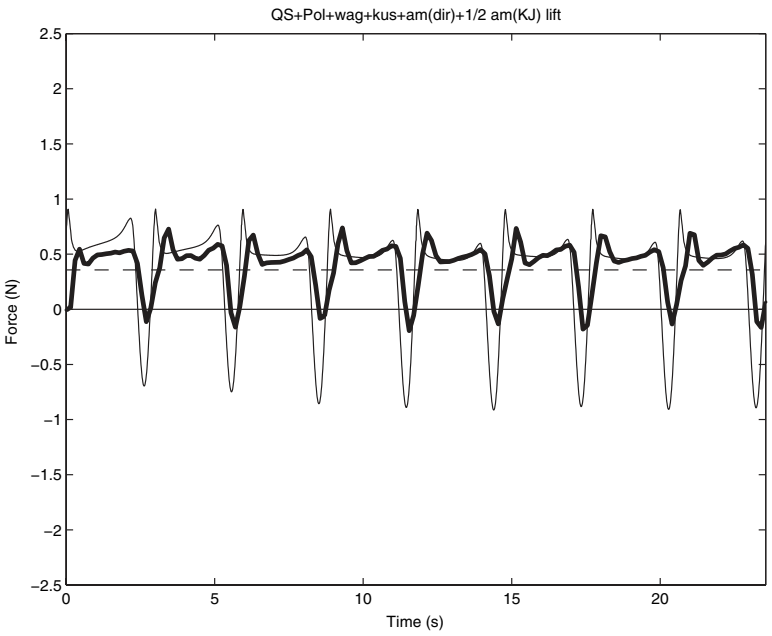


Figure 22: Total Robofly lift, including Dirichlet added mass forces, and half of the Kutta–Joukowski added mass force (thin line) versus measured Robofly lift (thick line); the dashed line is the average predicted force. Compare with Fig. 17.

Considering the total drag for all components apart from added mass in Fig. 27, it can be seen that the fit is poor: although the Polhamus effect correctly identifies the peak during each rotation, the magnitude of the force is overpredicted approximately by a factor of 2, just as for lift. The wake does not correct for this, because the Wagner effect does not affect drag in the model. Incorporating added mass (see Figs 28 and 29) correctly identifies the peaks at either end of the translation phase, but as with the vertical force, they are too large and too early, because the wake effects on the added mass forces are ignored.

The horizontal force model is not acceptably accurate without some refinement. Scaling the Polhamus effect was attempted, but due to the low rotation speeds, the scaling was 1 almost everywhere, with a few localised spikes of lower value at the rotations.

The average measured drag force was 0.60 N, the average predicted force was 1.00 N, an error of 67%.

### 9.2.1 Primary wake influence on drag

As can be seen from Figs 12, 14 and 26, the main effect of the wake is to reduce the predicted lift and drag forces at midstroke.

It is postulated that the major part of the error between the measured and predicted drag in Fig. 29 is due to the omission of primary wake (Wagner) effects on the drag (Fig. 30). From Fig. 31 it can be seen that the Wagner effect on lift is almost exactly opposite half of the combined quasi-steady and Polhamus lift. Effectively, the Wagner effect is halving the quasi-steady and Polhamus contributions to lift. Assuming a similar effect of the primary wake on drag gives the result of Fig. 32, which can be seen to be very close to the measured value. When using this correction, the average drag force was 0.41 N, an under-prediction of 32%. This method of

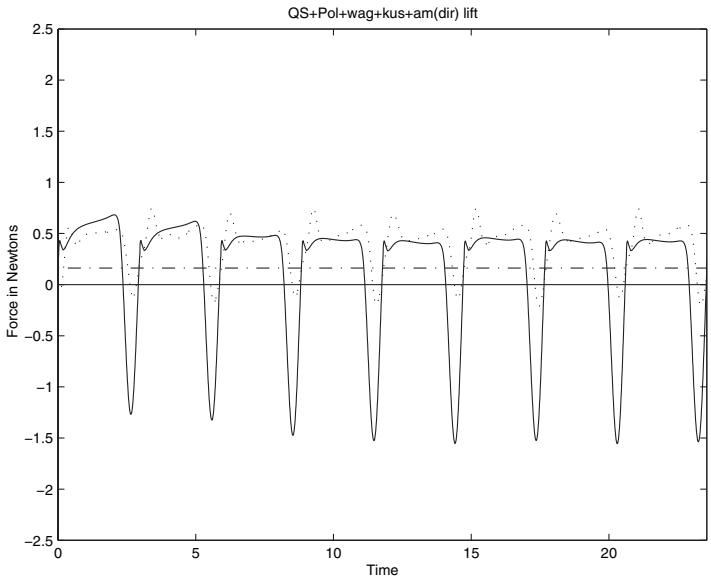


Figure 23: Robofly total lift with Dirichlet added mass correction, as in Fig. 19, but with *usepolhamus* = *'no'* (solid line) versus measured lift (dotted line). Note the loss of lift at reversal is much greater than in Fig. 19, and the 'bump' just before the reversal is lost. The chain line represents the average predicted force.

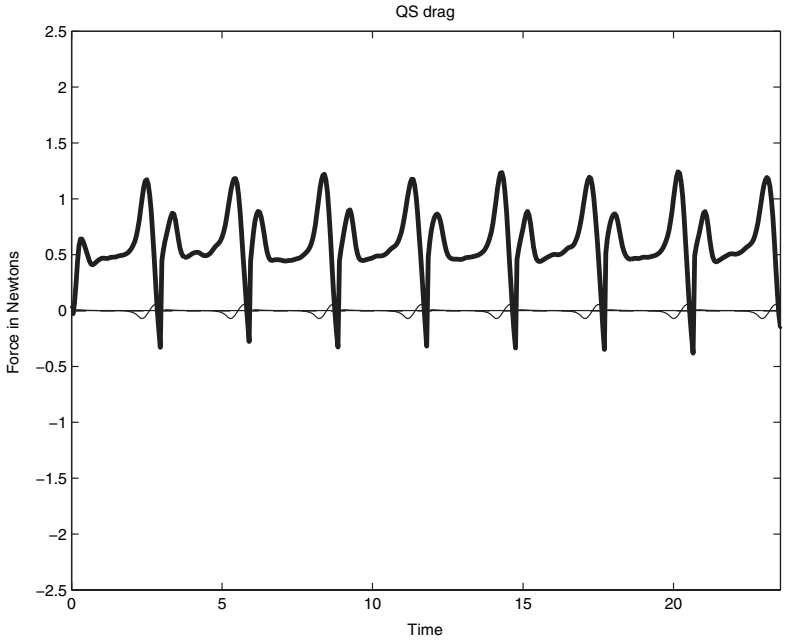


Figure 24: Quasi-steady drag, or absolute value of $F_{\mathrm{HQW}}$, (thin line) versus measured Robofly drag (thick line); the dashed line is the average predicted force.

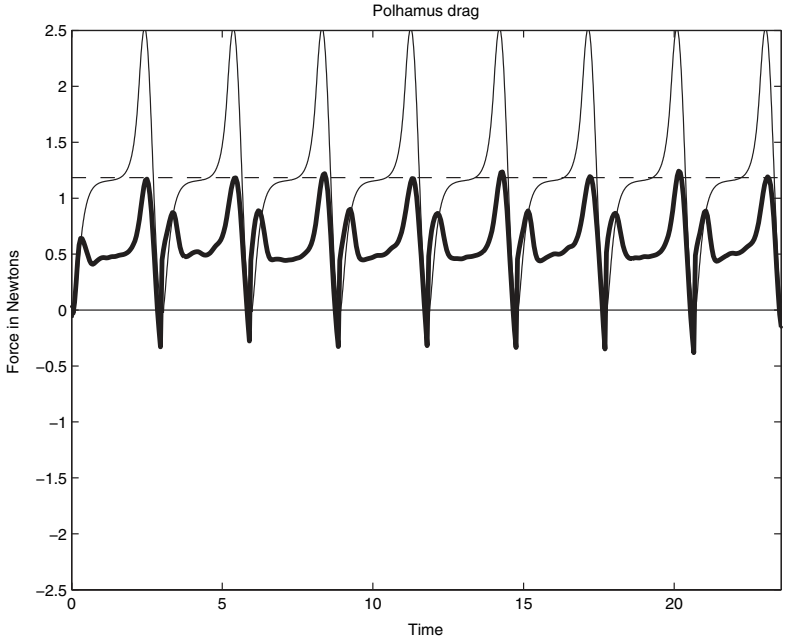


Figure 25: Polhamus correction to drag (thin line) versus measured Robofly drag (thick line); the dashed line is the average predicted force.

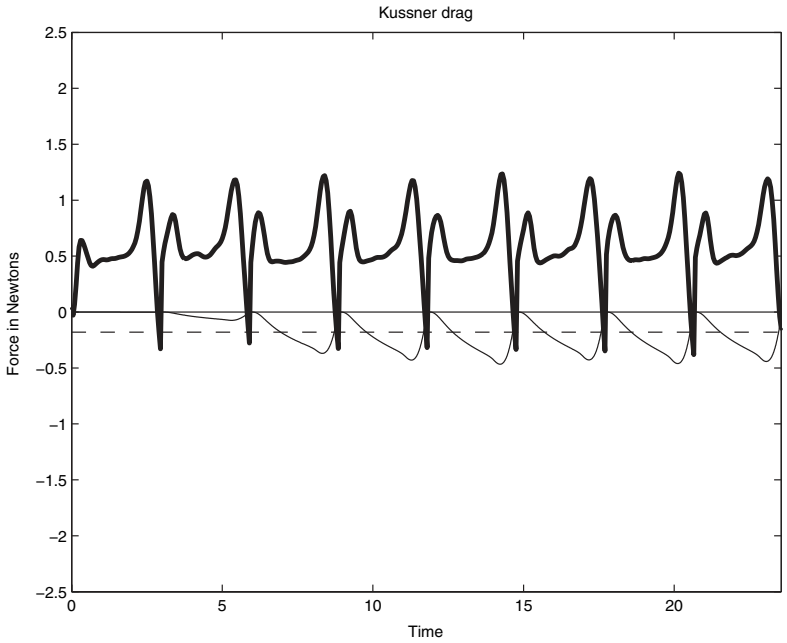


Figure 26: Secondary wake (Küssner) correction to drag (thin line) versus measured Robofly drag (thick line); the dashed line is the average predicted force.

primary wake correction for drag is too tenuous to be relied on. Note especially how it completely eliminates the first peak after reversal, because the primary wake effect should be delayed relative to the change in quasi-steady force. However, it does support the postulation that the major part of the error in predicted drag force is due to the omission of primary wake effects.

## 10 Discussion

### 10.1 Discussion of results

The Robofly data for both lift and drag show a similar form: a sharp trough near the reversal point, accompanied by peaks immediately before and after reversal. Between these two peaks (in the midstroke) the forces are lower, but increasing gradually towards the second peak.

For the predicted forces, both the lift and drag show a similar form: the Polhamus-corrected quasi-steady force overpredicts the measured force by a factor of 2, and has no first peak after reversal. The wake effect is to reduce these forces at midstroke. Finally, the added mass contribution has very little effect at midstroke, but causes a sharp reduction in forces at reversal and an increase immediately after, reducing the predicted value at reversal to match the trough in the measured data and introducing the first peak just after reversal, again to match the measured data.

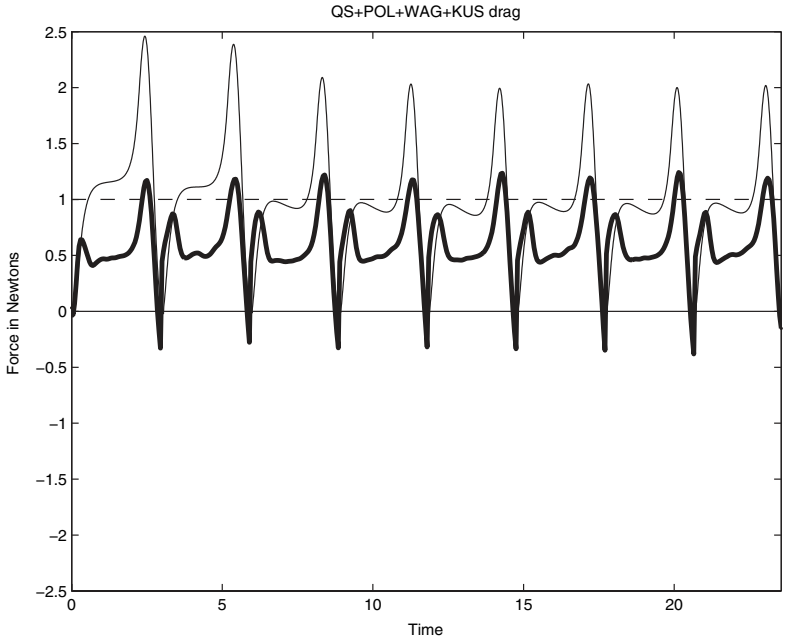


Figure 27: Total drag without added mass (thin line) versus measured Robofly drag (thick line); the dashed line is the average predicted force.

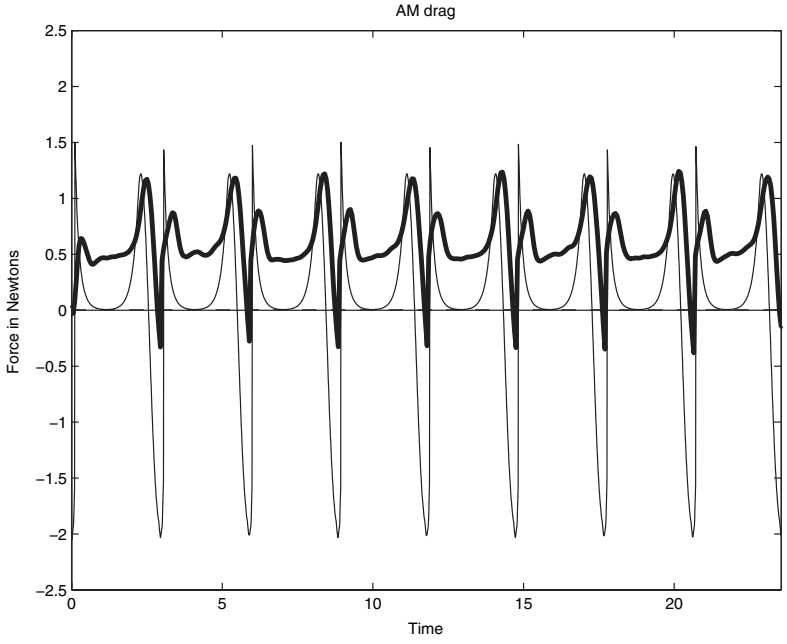


Figure 28: Added mass correction to drag (thin line) versus measured Robofly drag (thick line); the dashed line is the average predicted force.

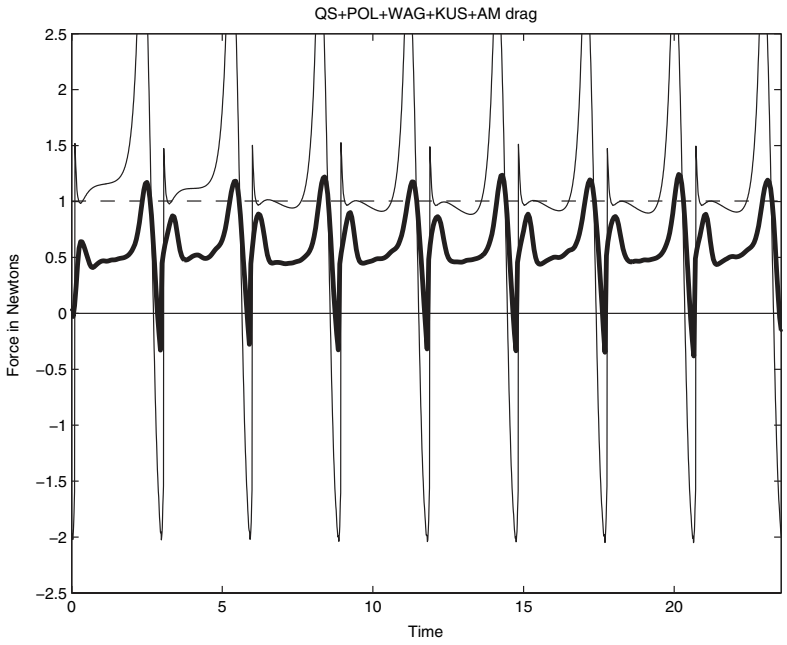


Figure 29: Total drag with added mass (thin line) versus measured Robofly drag (thick line); the dashed line is the average predicted force.

## 10.2 Evaluation of results

This section deals with the accuracy and utility of the model. It is concluded that the added mass model is not very good, as it overpredicts the effect of added mass by ignoring the effect of the primary wake on the added mass. The lift results are acceptable as a first-order model, in that they capture the general shape and overall scale of the lift force. Especially gratifying is the way they accurately capture the loss of lift due to the impulsive start. The drag results, however, are less good, primarily because our model predicts no effect of the primary wake on the drag force. The drag model also suffers from our fluid being modelled as inviscid, whereas most of the real-world drag in the experiment is viscous in origin. Using the Polhamus correction to force coefficient for the purpose of wake effect seems especially promising, but will require more validation, after the added mass model has been refined.

Moment data were not available for the Robofly experiment. This is unfortunate, as it makes it impossible to validate the expressions for the moments. The added mass moment is especially a concern, as the added mass forces were modelled without the effect of the wake. Similarly, the effect of omitting Polhamus corrections from the pitching moment cannot be evaluated.

Nonetheless, it is gratifying that a purely inviscid model has managed to get this close to experimental results, which are for a very viscous and unsteady flight regime. The model underpredicted the average lift by only 7.8%. Note also that the expected operating regime of the FMAV is considerably less viscous than that of Dickinson's experiment. Dickinson had a Reynolds number of order $10^2$, while for the MAV, the Reynolds number would be of the order of $10^5$.

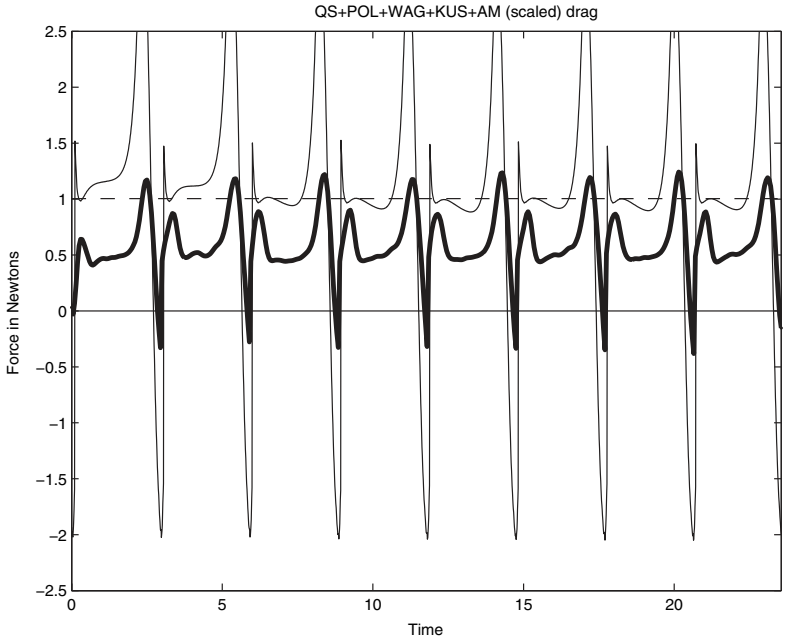


Figure 30: Total drag with added mass for Robofly dataset, including Dirichlet added mass forces, and half of the Kutta–Joukowski added mass force (thin line) versus measured Robofly drag (thick line); the dashed line is the average predicted force. Compare with Fig. 29.

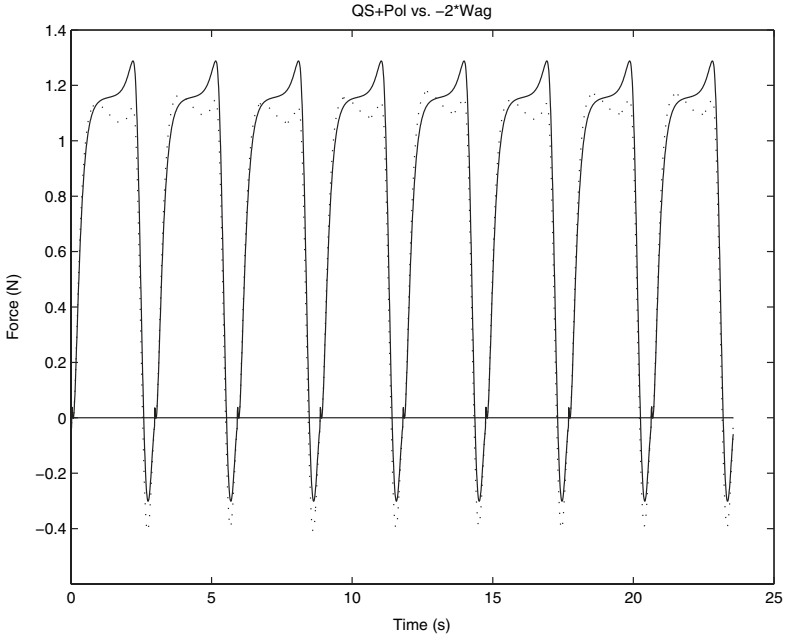


Figure 31: Comparison of predicted Polhamus-corrected quasi-steady lift (solid line) with minus twice the Wagner primary wake lift effect (dotted line). Note the strong correlation.

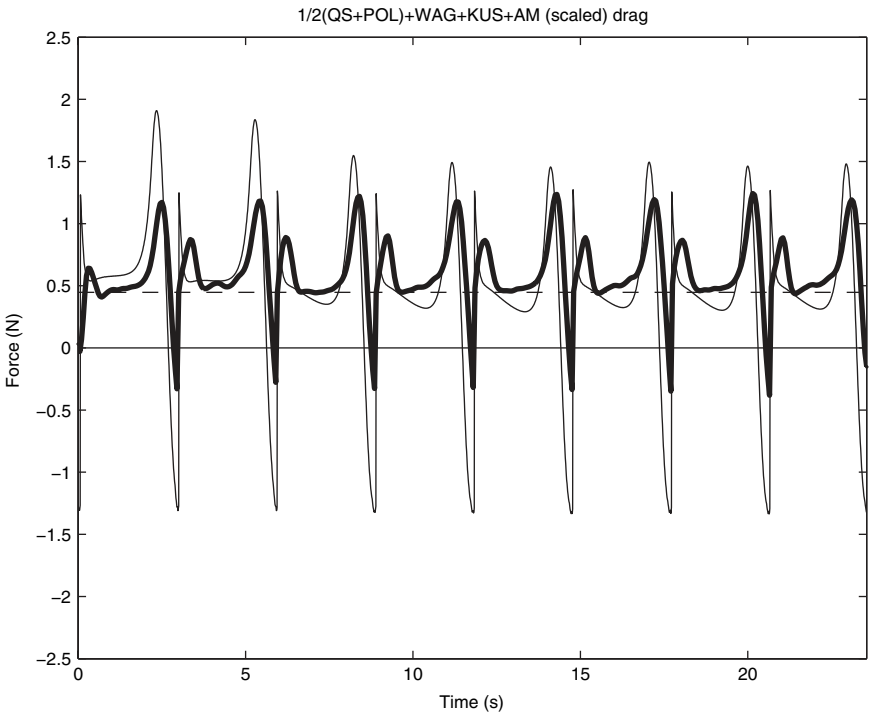


Figure 32: Total Robofly drag, as in Fig. 29, but minus half of quasi-steady and Polhamus contribution (thin line) versus measured drag (thick line); the dashed line represents the average predicted force.

## 11 Conclusions

### 11.1 Assumptions

- The wing root is stationary.
- The wing is thin and flat.
- The hinge point is at the same point on the chord for all spanwise sections, when wing shape factors are used.
- The body does not affect the airflow and is ignored.
- The far-field free stream is stationary.
- The flow is entirely inviscid.
- The flow separates sharply from the leading edge, causing total loss of leading edge suction.
- The flow always reattaches and forms a stable leading edge vortex.
- The effect of the leading edge vortex is to rotate the leading edge suction force by 90°, to become a normal force component.
- The direction of the above rotation is in the direction of the normal velocity at the leading edge.
- The leading edge vortex dissipates immediately when shed.
- The flow leaves the trailing edge smoothly, satisfying the Kutta–Joukowski condition.
- The wake is treated as a thin, globally stationary filament of vorticity.

- The wake does not decay or dissipate.
- The wake is split into single-stroke elements, each of which is assumed to be a straight line.
- The wake moves under constant downwash velocity $u_i$, without deforming under its own induced velocity.
- The above movement is discretised into a set of steps at each reversal.
- Each wake segment is assumed to be behind the wing until reversal, where all previous wakes jump downwards by a distance based on the average predicted downwash velocity.

### 11.2 Theory conclusions

A model has been developed for calculating highly unsteady lift of insect-like flapping wings, and embodied in MATLAB code. This model is analytic and modular, for the purpose of giving better insight into the various effects that act on the wing. However, this has come at the expense of considerable simplification, in order to enable the use of known solutions to standard unsteady problems. The main limitations of the model are: (1) no modelling of viscous forces (this was necessary to obtain an analytical potential model) and (2) the effect of the wake on added mass is incomplete: although the Küssner function includes the effect of added mass, the Wagner function does not.

The model was tested on the data from an experiment on Dickinson's Robofly from which it was concluded that the average circulatory lift predicted was within 7.8% of the measured. However, the non-circulatory lift (added mass effect) was a poor fit, so although added mass does not contribute a net force over a cycle, some features of the shape of the lift trace are lost, and the peak loads are being overpredicted. For drag, both the circulatory and non-circulatory component showed poor correlation. This is partly because of the above-mentioned problems with added mass, and the fact that the wake model does not model primary wake drag. However, it is also suspected to be mainly due to the fact that viscous drag is omitted entirely.

This model is based on several simplifications. These were made for the purpose of making it possible to embody the model in non-iterative code, and to give quantitative insight into the meaning of the results. Despite the simplifications, the time evolution of lift has been captured well and it has been shown that only the added mass component is not modelled with the required accuracy. This indicates the soundness of this modular approach.

## Appendix A: Terminology and notation

### A.1 Angle of attack

The angle of attack is usually defined as the angle between the mean chordline (the line from leading to trailing edge) and the free stream flow. It is not used in this investigation because: (1) wing rotation causes $\alpha$ to vary along the chord and (2) $\alpha$ is not small for the flapping wing.

Instead, the following calculations are performed as a function of the normal velocity directly, with no reference to $\alpha$. The wing attitude is obtained from the pitching angle $\beta$, which is defined from geometry and therefore independent of the free stream. For two examples of the relationship between $\alpha$ and the pitching and plunging motions, see Figs 33 and 34.

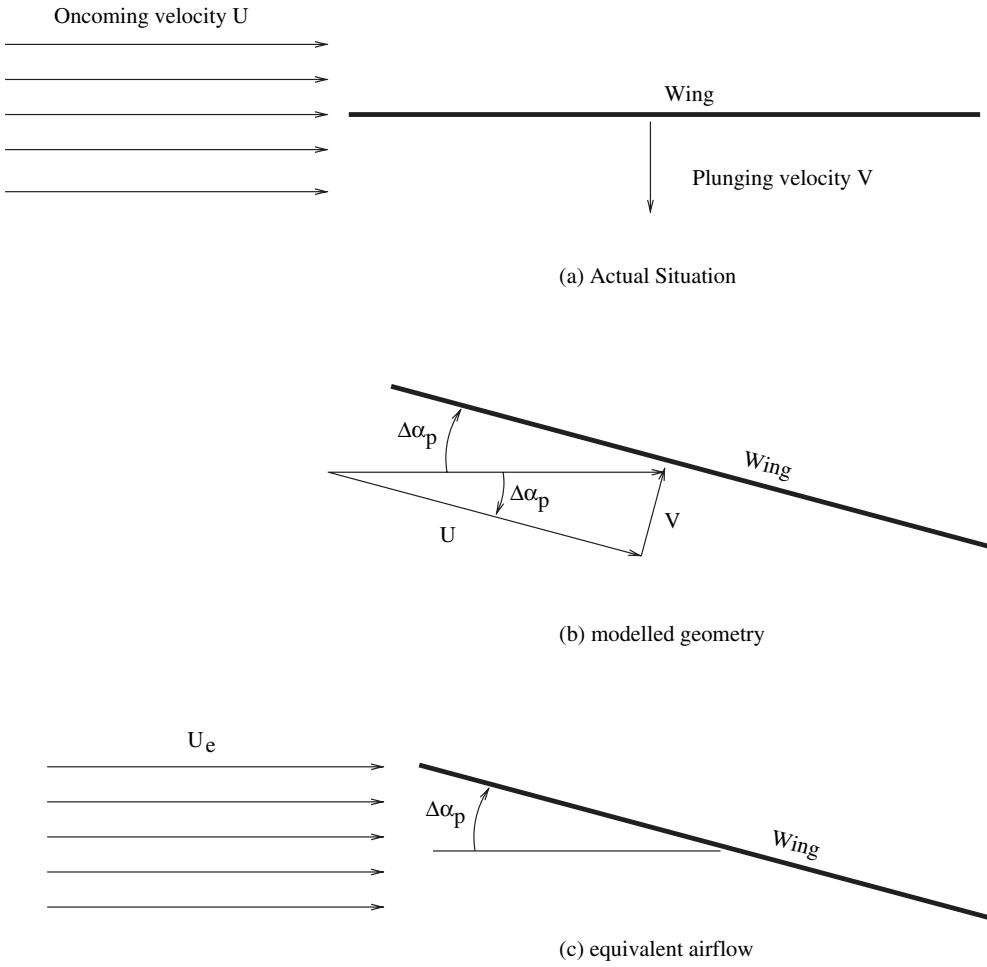


Figure 33: Illustration of the effect of plunging velocity correction on $\alpha$. Here $\Delta\alpha_p$ is the effective angle of attack due to plunging and differs from the geometric angle $\alpha$ which is zero.

### A.2 Velocities

Velocities are written in metres per second, as the velocity of the fluid relative to the wing, in the general form:

$$u_{123}.$$

The first subscript is the direction of the velocity:

- P is in the wing-fixed system, parallel to the wing, towards the trailing edge.
- N is in the wing-fixed system, normal to the wing, towards the 'upwards' side.
- V is in the spherical coordinate system, upwards (i.e. the $-\psi$ direction).
- H is in the spherical coordinate system, backwards (i.e. the $+\theta$ direction).
- **T** is the total velocity, in either coordinate system.

See Figs 38 and 39 for illustrations of the $-\psi$ and $+\theta$ directions.

The second subscript is the chordwise location of the velocity:

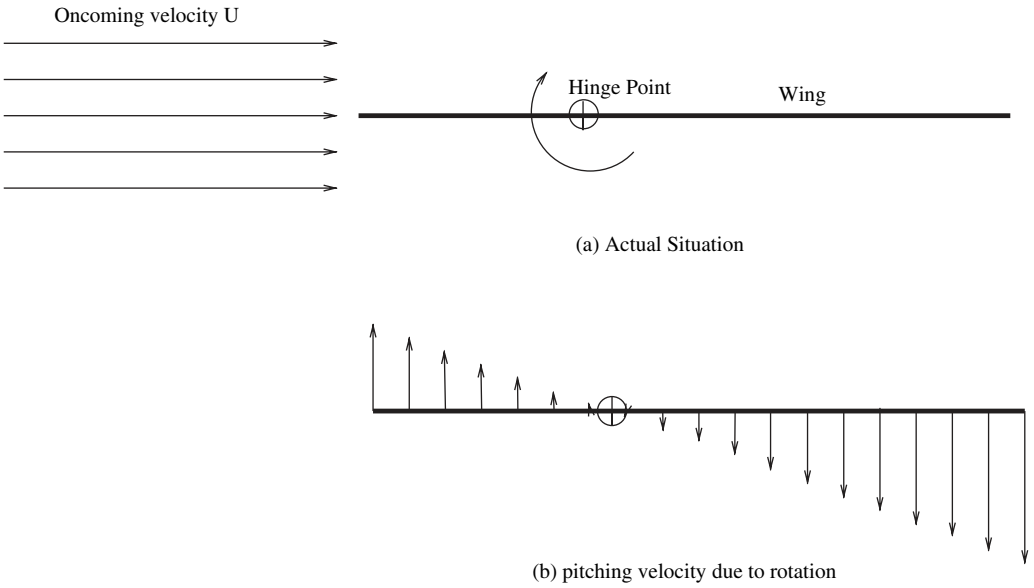


Figure 34: Pitching effect on normal velocity, and hence $\alpha$.

- $l$ is at the leading edge.
- $t$ is as the trailing edge.
- $m$ is at the midpoint.
- $r$ is at 3/4 chord, called the *rear neutral point*.

If this subscript is omitted, the velocity is assumed to be at the hinge point.

The third subscript is the spanwise position of the velocity:

- $T$ is at the tip of the wing, assumed on the hinge line.

If this subscript is omitted, the velocity is assumed to be at a radial position $r$.

Special case: The velocity $u_\mathrm{i}$ is the average downward velocity induced by the lift of the wing, it is positive downwards, i.e. the $+z$ direction.

### A.3 Forces

Forces are written in the general form:

$$F_{12\,33\,4}$$

If the fourth subscript is omitted, the force is assumed to be in Newtons per metre span (N/m), otherwise it is in Newtons (N). See below for details on this fourth subscript.

The first subscript is the direction of the force:

- P is in the wing-fixed system, parallel to the wing, towards the leading edge.
- N is in the wing-fixed system, normal to the wing, towards the 'upwards' side.
- V is in the spherical coordinate system, upwards (i.e. the $-\psi$ direction).
- H is in the spherical coordinate system, forwards (i.e. the $-\theta$ direction).
- L is in the rectangular coordinate system, upwards (i.e. the $-z$ direction).
- D is in the rectangular coordinate system, forwards (i.e. the $+x$ direction).

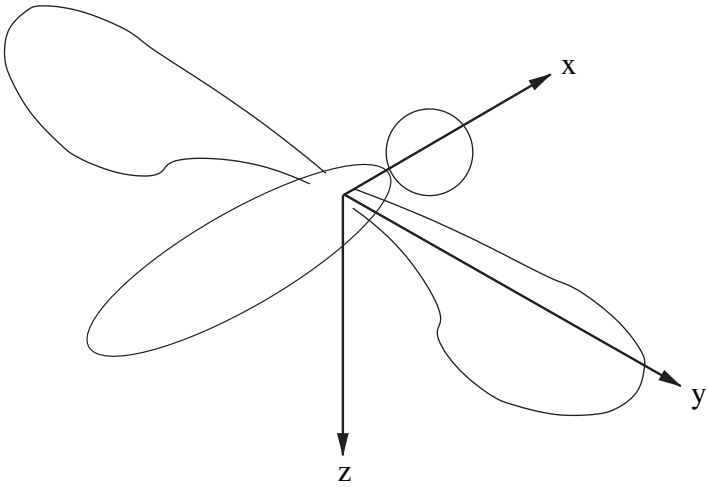


Axes origin at hinge point of wing

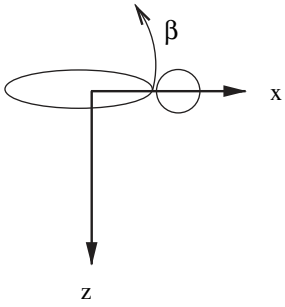


Pitching (supination). Seen from right wingtip.

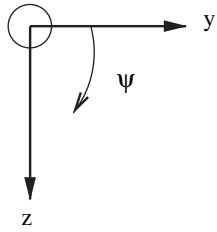


Plunging, seen from –X (behind).

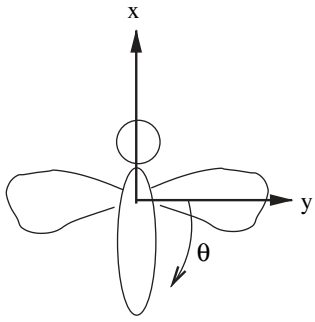


Sweeping, seen from –Z (above)

Figure 35: Coordinate system.

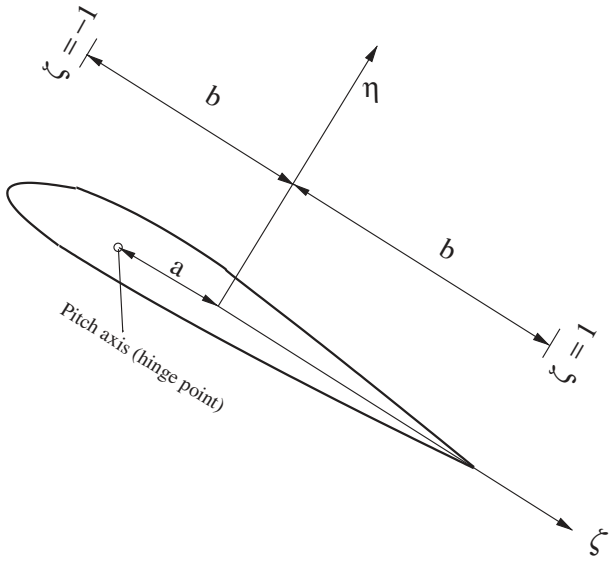


Figure 36: The wing-fixed coordinate system.

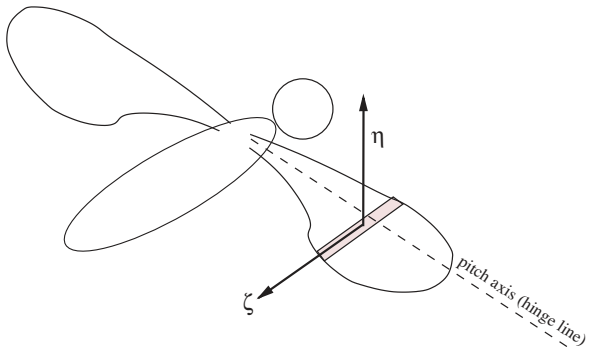


Figure 37: A sample wing section.

The relevant directions are shown in Figs 40 and 41.

The second subscript is the flow component causing the force:

- Q is quasi-steady.
- A is added mass.
- P is Polhamus effect.
- W is Wagner (primary wake).
- K is Küssner (secondary wakes).

If this subscript is omitted, the force is assumed to be the sum of all the above contributions.

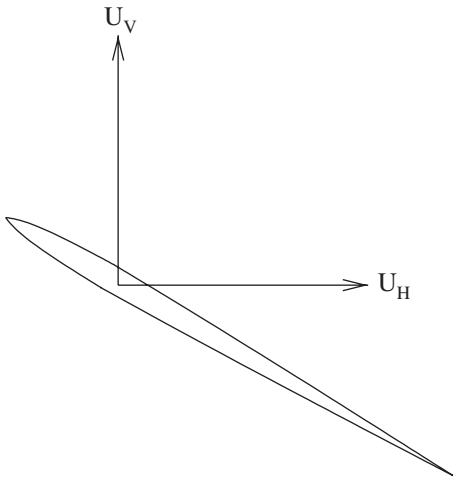


Figure 38: Direction of the horizontal velocity $u_H$ and the vertical velocity $u_V$, as seen from the root of the wing. These are defined as velocity of the fluid relative to the wing, in the spherical coordinate system.

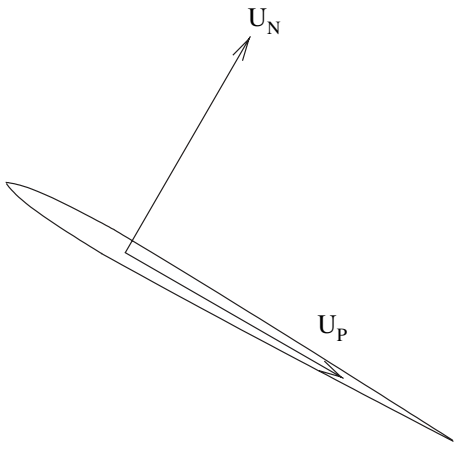


Figure 39: Direction of the normal velocity $u_N$ and the parallel velocity $u_P$, as seen from the root of the wing. These are defined as velocity of the fluid relative to the wing in the wing-fixed coordinate system of Fig. 36.

The third subscript may be one or two letters and is the component of the contribution for the quasi-steady and added mass terms only:

- TD is the translational component of the Dirichlet solution.
- RD is the rotational component of the Dirichlet solution.
- TK is the translational component of the Kutta–Joukowski correction.
- RK is the rotational component of the Kutta–Joukowski correction.
- D is the total Dirichlet solution.

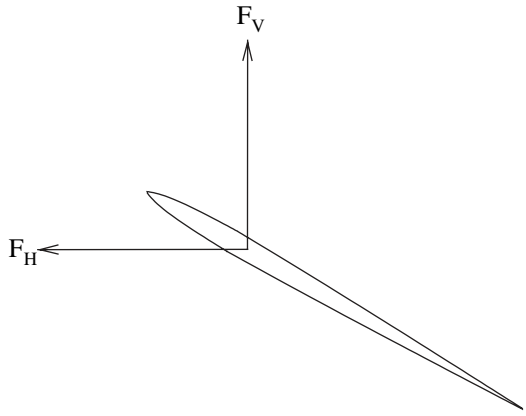


Figure 40: Direction of the horizontal force $F_H$ and the vertical force $F_V$, as seen from the root of the wing, in the spherical coordinate system.

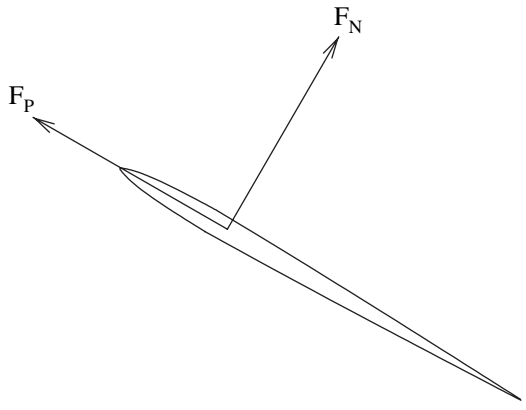


Figure 41: Direction of the normal force $F_N$ and the parallel force $F_P$, as seen from the root of the wing, in the wing-fixed coordinate system of Fig. 36.

- K is the total Kutta–Joukowski correction.

If this subscript is omitted, the force is assumed to be for the total contribution of all components. The fourth, optional, subscript denotes the area of integration:

- W means the force is integrated over the entire wing.

If this subscript is omitted, the force is assumed to be per metre span.
The shorthand 'lift' is used for the vertical force $F_V$ and 'drag' for the horizontal force $F_H$.

### A.4 Moments

Moments are written in the general form:

$$M_{12\,33\,4}$$

If the fourth subscript is omitted, the moment is assumed to be in Newton-metres per metre span (Nm/m), otherwise it is in Newton-metres (Nm). See below for details on this fourth subscript.

The subscripts are similar to those for forces above, except the first, where the only cases are:

- V Moment about the $x$ axis, positive in the $-\psi$ direction (upwards).
- H Moment about the $z$ axis, positive in the $-\theta$ direction (forwards).
- P Pitching moment about the hinge line, positive in the $+\beta$ (pitching up).

The descriptions of direction ('upwards', and so on) are local to the right-hand wing, which is the only one considered.

### A.5 Other definitions

| | |
|---|---|
| $Q$ | $\sqrt{1-\zeta^2}$ |
| $\mathbf{C}$ | cos |
| $\mathbf{S}$ | sin |
| $\mathbf{S}^m_{n\alpha}$ | $\sin(n\alpha)^m$ |
| $\mathrm{T_P}$ | Polhamus-effect turn direction, see eqn (102) |
| $\varphi$ | wing sweep factor, see p. 27 |

#### A.5.1 Downwash velocity $u_\mathrm{i}$

Any lift generation causes a downwash velocity, and the Rankine–Froude theory for an actuator disc assumes a constant downwash velocity $u_\mathrm{i}$ across the swept disc of a propeller. In hover this yields:

$$u_\mathrm{i} = \sqrt{\frac{\bar{F}}{2\rho A_\mathrm{S}}}, \tag{118}$$

where $\bar{F}$ is the average lift force, and $A_\mathrm{S}$ is the *swept area* of the propeller, the horizontal area that the wing passes over during a stroke. This is shown in Fig 42. Note on the same figure the important issue of a partial actuator disc. The left-hand figure shows the full area within the wing tip radius, which is the swept area when the wing performs full rotations and passes over the entire disc. For our application, however, $A_\mathrm{S}$ is based on the area each wing will actually traverse over during a stroke, as shown in the right-hand figure.

### A.6 Basic identities

On the basis of the above definitions, some basic identities are available:

$$u_\mathrm{H} = -Rr\dot{\theta}, \tag{119}$$

$$u_\mathrm{V} = Rr\dot{\psi}, \tag{120}$$

$$u_\mathrm{N} = u_\mathrm{H}\mathbf{S}_\beta + u_\mathrm{V}\mathbf{C}_\beta, \tag{121}$$

$$u_\mathrm{P} = u_\mathrm{H}\mathbf{C}_\beta - u_\mathrm{V}\mathbf{S}_\beta, \tag{122}$$

see Fig. 35. Note the minus sign in the first equation, since velocity is defined in terms of the free stream velocity relative to the wing, so the velocities above are the opposite to those of the wing in still air. The last two equations are simply from resolving velocities in the spherical coordinate system to the wing-local system.

The above equations can be used to find the velocities at local points of the wing. The subscript E is used for an arbitrary point on the wing. The local wing semichord is $b$, and the hinge location in wing-fixed coordinates is $a$:

$$u_{\mathrm{PE}} = u_{\mathrm{P}}, \tag{123}$$

$$u_{\mathrm{NE}} = u_{\mathrm{N}} + b\dot{\beta}(\zeta - a), \tag{124}$$

$$u_{\mathrm{Nl}} = u_{\mathrm{N}} + b\dot{\beta}(-1 - a), \tag{125}$$

$$u_{\mathrm{Nm}} = u_{\mathrm{N}} + b\dot{\beta}(-a), \tag{126}$$

$$u_{\mathrm{Nr}} = u_{\mathrm{N}} + b\dot{\beta}(\tfrac{1}{2} - a), \tag{127}$$

$$u_{\mathrm{Nt}} = u_{\mathrm{N}} + b\dot{\beta}(1 - a). \tag{128}$$

Equation (123) indicates that, in the wing-fixed coordinate system, the rotational velocity will manifest itself purely as a normal component. Equations (125)–(128) are just special cases of eqn (124). Also, all velocities at the hinge will scale linearly with the radius:

$$u = r u_{\mathrm{T}}. \tag{129}$$

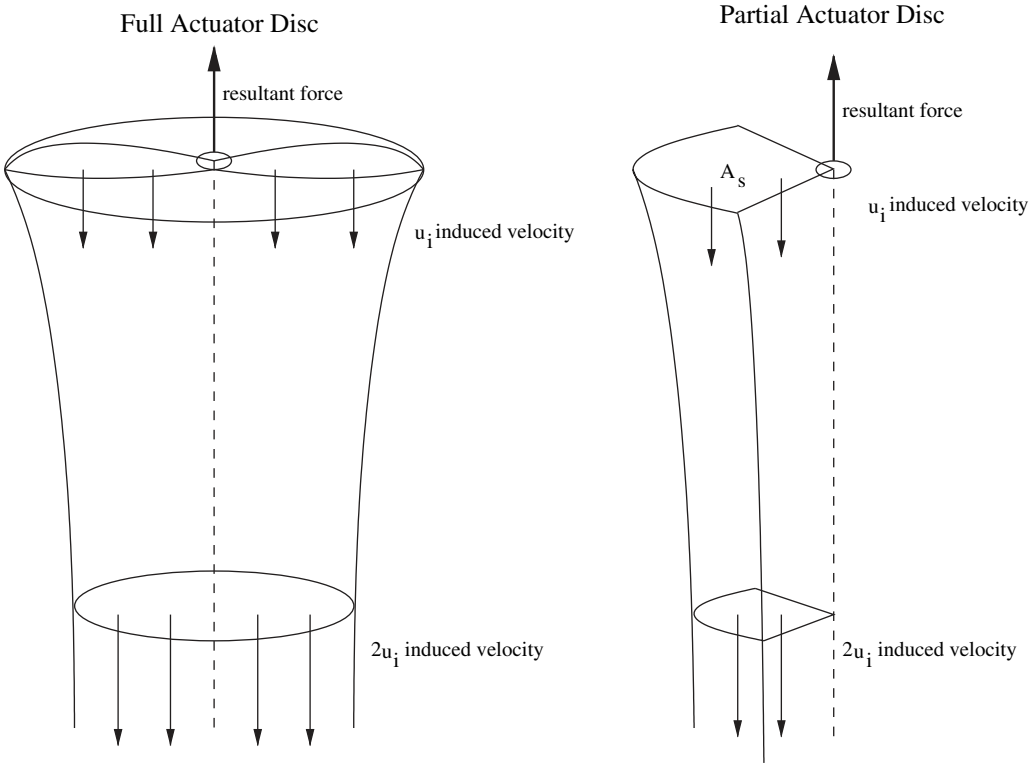


Figure 42: Swept area used to determine induced velocity, based on momentum theory, after [11].

Some basic identities can be formed for forces by resolving between coordinate systems:

$$F_{\mathrm{V}} = F_{\mathrm{N}}\mathbf{C}_{\beta} + F_{\mathrm{P}}\mathbf{S}_{\beta}, \tag{130}$$

$$F_{\mathrm{H}} = -F_{\mathrm{N}}\mathbf{S}_{\beta} + F_{\mathrm{P}}\mathbf{C}_{\beta}, \tag{131}$$

$$F_{\mathrm{N}} = F_{\mathrm{V}}\mathbf{C}_{\beta} - F_{\mathrm{H}}\mathbf{S}_{\beta}, \tag{132}$$

$$F_{\mathrm{P}} = F_{\mathrm{V}}\mathbf{S}_{\beta} + F_{\mathrm{H}}\mathbf{C}_{\beta}, \tag{133}$$

$$F_{\mathrm{L}} = F_{\mathrm{V}}\mathbf{C}_{\psi}, \tag{134}$$

$$F_{\mathrm{D}} = F_{\mathrm{H}}\mathbf{C}_{\theta}, \tag{135}$$

The last two equations are the forces experienced by the body in the rectangular coordinate system. Also, the definition of 'drag' makes it always positive forwards and spanwise forces have been ignored. In the spherical coordinate system the model used predicts no spanwise force (see the Polhamus model in Section 5). In the rectangular coordinate system any spanwise force caused by one wing is assumed to be cancelled by the opposite wing, due to symmetry.

## Acknowledgements

This work has been supported by the UK Engineering and Physical Sciences Research Council (EPSRC) through Grants GR/M22970 and GR/M78472. The latter has been co-funded by the UK Ministry of Defence.

The data used in this report were kindly made available by Prof. Michael Dickinson and Dr. William Dickson of the California Institute of Technology from their Robofly project.

## References

[1] Żbikowski, R., Flapping wing autonomous micro air vehicles: Research programme outline. *Fourteenth International Conference on Unmanned Air Vehicle Systems*, volume [Supplementary Papers], pp. 38.1–38.5, 1999.

[2] Żbikowski, R., Flapping wing micro air vehicle: a guided platform for microsensors. *Royal Aeronautical Society Conference on Nanotechnology and Microengineering for Future Guided Weapons*, pp. 1.1–1.11, 1999.

[3] Żbikowski, R., Flapping wing technology. *European Military Rotorcraft Symposium*, Shrivenham, UK, 21–23 March 2000, pp. 1–7, 2000.

[4] Żbikowski, R., On aerodynamic modelling of an insect-like flapping wing in hover for micro air vehicles. *Philosophical Transactions of the Royal Society of London (Series A: Mathematical, Physical and Engineering Sciences)*, **360(1791)**, pp. 273–290, 2002.

[5] Pedersen, C.B., An indicial-Polhamus model of aerodynamics of insect-like flapping wings in hover. PhD thesis, Cranfield University, Royal Military College of Science (RMCS) Shrivenham, 2003.

[6] Pringle, J.W.S., *Insect Flight*, Vol. 52, Oxford Biology Readers, Oxford University Press: Glasgow, 1975.

[7] Ellington, C.P., The aerodynamics of hovering insect flight. I. The quasi-steady analysis. *Philosophical Transactions of the Royal Society of London Series B Biological Sciences*, **305(1122)**, pp. 1–15, 1984.

[8] Ellington, C.P., The aerodynamics of hovering insect flight. II. Morphological parameters. *Philosophical Transactions of the Royal Society of London Series B Biological Sciences*, **305(1122)**, pp. 17–40, 1984.
[9] Ellington, C.P., The aerodynamics of hovering insect flight. III. Kinematics. *Philosophical Transactions of the Royal Society of London Series B Biological Sciences*, **305(1122)**, pp. 41–78, 1984.
[10] Ellington, C.P., The aerodynamics of hovering insect flight. IV. Aerodynamic mechanisms. *Philosophical Transactions of the Royal Society of London Series B Biological Sciences*, **305(1122)**, pp. 79–113, 1984.
[11] Ellington, C.P., The aerodynamics of hovering insect flight. V. A vortex theory. *Philosophical Transactions of the Royal Society of London Series B Biological Sciences*, **305(1122)**, pp. 115–144, 1984.
[12] Ellington, C.P., The aerodynamics of hovering insect flight. VI. Lift and power requirements. *Philosophical Transactions of the Royal Society of London Series B Biological Sciences*, **305(1122)**, pp. 145–181, 1984.
[13] Ellington, C.P., van den Berg, C., Willmott, A.P. & Thomas, A.L.R., Leading-edge vortices in insect flight. *Nature*, **384(6610)**, pp. 626–630, 1996.
[14] Willmott, A.P., Ellington, C.P. & Thomas, A.L.R., Flow visualization and unsteady aerodynamics in the flight of the hawkmoth, *Manduca sexta*. *Philosophical Transactions of the Royal Society of London Series B Biological Sciences*, **352(1351)**, pp. 303–316, 1997.
[15] van den Berg, C. & Ellington, C.P., The vortex wake of a 'hovering' model hawkmoth. *Philosophical Transactions of the Royal Society of London Series B Biological Sciences*, **352(1351)**, pp. 317–328, 1997.
[16] van den Berg, C. & Ellington, C.P., The three-dimensional leading-edge vortex of a 'hovering' model hawkmoth. *Philosophical Transactions of the Royal Society of London Series B Biological Sciences*, **352(1351)**, pp. 329–340, 1997.
[17] Birch, J.M. & Dickinson, M.H., Spanwise flow and the attachment of the leading-edge vortex on insect wings. *Nature*, **412(6848)**, pp. 729–733, 2001.
[18] Crighton, D.G., The Kutta condition in unsteady flow. *Annual Review of Fluid Mechanics*, **17**, pp. 411–445, 1985.
[19] Silverstein, A. & Joyner, U.T., Experimental verification of the theory of oscillating airfoils. NACA Report 673, National Advisory Committee for Aeronautics, 1939.
[20] Houghton, E.L. & Carpenter, P.W., *Aerodynamics for Engineering Students*, Edward Arnold: London, 4th edn, 1993.
[21] Kuethe, A.M. & Chow, C.Y., *Foundations of Aerodynamics. Bases of Aerodynamic Design*, John Wiley & Sons: New York, 5th edn, 1998.
[22] McCroskey, W.J., The phenomenon of dynamic stall. NASA Technical Memorandum TM-81264, National Aeronautics and Space Administration, 1981.
[23] Leishman, J.G., *Principles of Helicopter Aerodynamics*, Cambridge University Press: Cambridge, England, 2000.
[24] Polhamus, E.C., A concept of the vortex lift of sharp-edge delta wings based on a leading-edge-suction analogy. NASA Technical Note TN D-3767, National Aeronautics and Space Administration, 1966.
[25] Wagner, H., Über die Entstehung des dynamischen Auftriebes von Tragflügeln. *Zeitschrift für Angewandte Mathematik und Mechanik*, **5(1)**, pp. 17–35, 1925.
[26] Küssner, H.G., Zusammenfassender Bericht über den instationären Auftrieb von Flügeln. *Luftfahrtforschung*, **13(12)**, pp. 410–424, 1936.

[27] Loewy, R.G., A two-dimensional approximation to the unsteady aerodynamics of rotary wings. *Journal of the Aeronautical Sciences*, **24(2)**, pp. 81–92, 144, 1957.
[28] Sane, S.P., The aerodynamics of insect flight. *Journal of Experimental Biology*, **206(23)**, pp. 4191–4208, 2003.
[29] Rozhdestvensky, K.V. & Ryzhov, V.A., Aerohydrodynamics of flapping-wing propulsors. *Progress in Aerospace Sciences*, **39(8)**, pp. 585–633, 2003.
[30] Lehmann, F.O., The mechanisms of lift enhancement in insect flight. *Naturwissenschaften*, **91(3)**, pp. 101–122, 2004.
[31] Walker, J.A., Rotational lift: something different or more of the same? *Journal of Experimental Biology*, **205(24)**, pp. 3783–3792, 2002.
[32] Minotti, F.O., Unsteady two-dimensional theory of a flapping wing. *Physical Review E*, **66(5)**, p. 5, 2002. Article number: 051907-1-051907-10.
[33] Katz, J. & Plotkin, A., *Low Speed Aerodynamics*, Cambridge University Press: New York, 2nd edn, 2001.
[34] von Kármán, T. & Sears, W.R., Airfoil theory for non-uniform motion. *Journal of the Aeronautical Sciences*, **5(10)**, pp. 379–390, 1938.
[35] Theodorsen, T., General theory of aerodynamic instability and the mechanism of flutter. NACA Report 496, National Advisory Committee for Aeronautics, 1935.
[36] Stokes, G.G., On the effect of the internal friction of fluids on the motion of pendulums. *Transactions of Cambridge Philosophical Society*, **9**, pp. 8–106, 1851.
[37] Massey, B.S., *Mechanics of Fluids*, Chapman and Hall: London, 7th edn, 1998.
[38] Newman, J.N., *Marine Hydrodynamics*, MIT Press: London, England, 1977.
[39] Milne-Thomson, L.M., *Theoretical Hydrodynamics*, Dover: Mineola, NY, 5th edn, 1996.
[40] Sedov, L.I., *Two-Dimensional Problems in Hydrodynamics and Aerodynamics*, Wiley: London, England, 1965.
[41] Lamar, J.E., The use and characteristics of vortical flows near a generating aerodynamic surface: A perspective. *Progress in Aerospace Science*, **34(3–4)**, pp. 167–217, 1998. (Erratum in Volume 34, Number 7–8, page 543).
[42] Bradley, R.G., Smith, C.W. & Bhateley, I.C., Vortex-lift prediction for complex wing planforms. *Journal of Aircraft*, **10(6)**, pp. 379–381, 1973.
[43] Sane, S.P. & Dickinson, M.H., The aerodynamic effects of wing rotation and a revised quasi-steady model of flapping flight. *Journal of Experimental Biology*, **205(8)**, pp. 1087–1096, 2002.
[44] Sane, S.P. & Dickinson, M.H., The control of flight force by a flapping wing: Lift and drag production. *Journal of Experimental Biology*, **204(19)**, pp. 2607–2625, 2001. (Erratum in **204(19)**, 3401.)
[45] Dickinson, M.H., Lehmann, F.O. & Sane, S.P., Wing rotation and the aerodynamic basis of insect flight. *Science*, **284(1)**, pp. 1954–1960, 1999.
[46] DeLaurier, J.D., An aerodynamic model for flapping-wing flight. *The Aeronautical Journal*, **97**, pp. 125–130, 1993.